

Chapter 3

Advanced Polarimetric Concepts

Since the introduction of polarimetric radar data in the 1980s, many different analysis techniques have been investigated. Many of these are application specific. In this chapter we shall discuss the theoretical background for many of these techniques and compare the information that is provided by the different approaches. As we shall see, many of these techniques provide very similar information, with the result that the choice of analysis technique becomes more one of personal preference.

3.1 Vector-Matrix Duality of Scatterer Representation

In the previous Chapter we demonstrated that the received power can be written in terms of the scatterer covariance matrix, as follows:

$$P = \mathbf{A} \cdot [\mathbf{C}] \mathbf{A}^* ; \quad [\mathbf{C}] = \mathbf{T} \tilde{\mathbf{T}}^* \quad (3.1-1)$$

The superscript * denotes complex conjugation and ~ denotes the transpose operation. The vector \mathbf{T} contains the same information as the original scattering matrix.

If we restrict ourselves to the backscatter direction where $S_{hv} = S_{vh}$, the usual forms for the antenna and scatterer vectors are

$$\tilde{\mathbf{A}} = \begin{pmatrix} p_h^{rec} & p_h^{tr} & 1/\sqrt{2} \{ p_h^{rec} p_v^{tr} + p_v^{rec} p_h^{tr} \} & p_v^{rec} & p_v^{tr} \end{pmatrix}$$

and

$$\tilde{\mathbf{T}} = \begin{pmatrix} S_{hh} & \sqrt{2} S_{hv} & S_{vv} \end{pmatrix}.$$

The covariance matrix as defined in this expression is a positive semi-definite Hermetian matrix. This means that all the eigenvalues are real and that the eigenvectors are orthogonal. To prove that the eigenvalues have to be non-negative, recall that we can diagonalize the covariance matrix using a unitary transformation, as follows

$$[\mathbf{\Lambda}] = [\mathbf{U}]^{-1} [\mathbf{C}] [\mathbf{U}]. \quad (3.1-2)$$

In this equation, $[\mathbf{\Lambda}]$ is a 3×3 diagonal matrix containing the non-negative real eigenvalues of the covariance matrix and $[\mathbf{U}]$ is a 3×3 complex matrix with columns equal to the normalized eigenvectors of the covariance matrix. Because the covariance matrix is Hermitian, however, the matrix $[\mathbf{U}]$ also satisfies

$$[\mathbf{U}]^\dagger [\mathbf{U}] = [\mathbf{I}] \Rightarrow [\mathbf{U}]^\dagger = [\mathbf{U}]^{-1}, \quad (3.1-3)$$

where the \dagger sign denotes the adjoint (complex conjugate transpose) of the matrix. The normalized eigenvectors (or their complex conjugates) form an orthonormal basis; we can, therefore, write any antenna vector as a linear combination of these vectors. Specifically,

$$\mathbf{A} = b_1 \hat{\mathbf{e}}_1^* + b_2 \hat{\mathbf{e}}_2^* + b_3 \hat{\mathbf{e}}_3^* = [\mathbf{U}]^* \mathbf{B}. \quad (3.1-4)$$

Using Eq. (3.1-4) in Eq. (3.1-1), we find the following expression for the power

$$P = [\mathbf{U}]^* \mathbf{B} \cdot [\mathbf{C}] [\mathbf{U}] \mathbf{B}^* = \mathbf{B} \cdot [\mathbf{U}]^{-1} [\mathbf{C}] [\mathbf{U}] \mathbf{B}^* = |b_1|^2 \lambda_1 + |b_2|^2 \lambda_2 + |b_3|^2 \lambda_3 \geq 0. \quad (3.1-5)$$

The received power must be non-negative for all antenna vectors, which means that all the eigenvalues must be non-negative.

In the case where the covariance matrix represents a single scatterer (that is, it was calculated from a scattering matrix, as shown in Eq. (3.1-1)), it is easy to show that the eigenvalues are

$$\lambda_1 = S_{hh} S_{hh}^* + S_{vv} S_{vv}^* + 2S_{hv} S_{hv}^*, \lambda_2 = \lambda_3 = 0. \quad (3.1-6)$$

In this case, two of the three eigenvalues are zero. This, in fact, is the test of whether one could calculate an equivalent scattering matrix from any given covariance matrix.

The covariance matrix characterization is particularly useful when analyzing multi-look radar images, since the covariance matrix of a multi-look pixel is simply the average covariance matrix of all the individual measurements

contained in the multi-look pixel. Recall that multi-looking is performed by averaging the power from adjacent pixels together in order to reduce speckle. This averaging process can be written as

$$\langle P \rangle = \frac{1}{MN} \sum_{j=1}^M \sum_{i=1}^N P_{ij} = \frac{1}{MN} \sum_{j=1}^M \sum_{i=1}^N \mathbf{A} \cdot [C]_{ij} \mathbf{A}^* = \mathbf{A} \cdot \langle [C] \rangle \mathbf{A}^*, \quad (3.1-7)$$

where the two subscripts denote averaging in the range and azimuth directions, respectively. The angular brackets $\langle \rangle$ denote this spatial averaging. In general, this average covariance matrix will have more than one non-zero eigenvalue. All eigenvalues must, however, still be non-negative.

Cloude (1992) [1] was the first to use the orthonormality of the eigenvectors of the covariance matrix (in the context of radar polarimetry) to propose the decomposition of the covariance matrix in terms of its eigenvalues and eigenvectors. Specifically:

$$\langle [C] \rangle = \sum_{i=1}^3 \lambda_i \hat{\mathbf{e}}_i \hat{\mathbf{e}}_i^\dagger. \quad (3.1-8)$$

The decomposition proposed by Cloude [1], as shown in Eq. (3.1-8), is unique. That is, since the eigenvectors of the covariance matrix are orthogonal, they form a natural basis in which to express the scattering. In some sense, this breaks the covariance matrix into orthogonal components, as one would normally do for a vector. However, as a vector can be expressed in many different coordinate systems, so too can a covariance matrix. For example, we could also choose to write the average covariance matrix in the following form

$$\langle [C] \rangle = \sum_{i=1}^3 w_i \hat{\mathbf{p}}_i \hat{\mathbf{p}}_i^\dagger, \quad (3.1-9)$$

where the vectors $\hat{\mathbf{p}}_i$ form an orthonormal set. An example of such a set is the vectors representing the Pauli spin matrices:

$$\hat{\mathbf{p}}_1 = \frac{1}{\sqrt{2}} \begin{pmatrix} 1 \\ 0 \\ 1 \end{pmatrix}; \quad \hat{\mathbf{p}}_2 = \frac{1}{\sqrt{2}} \begin{pmatrix} 1 \\ 0 \\ -1 \end{pmatrix}; \quad \hat{\mathbf{p}}_3 = \begin{pmatrix} 0 \\ 1 \\ 0 \end{pmatrix}. \quad (3.1-10)$$

Note that any set of orthonormal vectors can be used when decomposing the averaged covariance matrix. Just as in the vector case, the choice of coordinate system depends on the application. In the case of the covariance matrix, this

choice is often dictated by the fact that we are trying to interpret the total scattering in terms of known models or scattering mechanisms. For example, the three Pauli vectors represent scattering from a metallic trihedral corner reflector, a metallic dihedral corner reflector, and a metallic dihedral corner reflector rotated by 45 degrees (deg) about the line of sight, respectively, as discussed in Chapter 2.

The Cloude eigenvector decomposition is a special case of the general decomposition. While it is mathematically unique, its interpretation is not necessarily straightforward. The reason for this is that there is no guarantee that the eigenvectors will represent any known physical scattering mechanism directly. An additional complication comes from the fact that if this decomposition is done on every pixel in a multi-looked image, the eigenvectors that form the coordinate system for this decomposition might be different from pixel to pixel. This means that the coordinate system generally varies from pixel-to-pixel unless all the covariance matrices have identical eigenvectors. Therefore, the value of any eigenvalue might vary from pixel to pixel, and it is not easy to tell if the variation is due to the strength of the scattering or to the fact that the eigenvectors are different. One common way to reduce this problem is to express the scattering vector in the Pauli basis and then calculate the equivalent covariance matrix and perform the decomposition in this basis. This does not, however, actually overcome the fundamental issue of the coordinate system varying from pixel to pixel; instead, this approach facilitates interpreting the eigenvectors in terms of Pauli vectors.

Many authors have proposed so-called target decomposition schemes in which a covariance matrix is decomposed into separate matrices on the basis of simple models. In those cases, care must be taken to ensure that the individual matrices that are used in the decomposition all satisfy the condition that their individual eigenvalues must be non-negative. We shall discuss this further in a later section.

Whether one thinks of a scatterer in terms of a covariance matrix or a set of scattering vectors is a matter of personal choice. In the rest of this chapter we shall explore various interpretations of the average scattering based on different applications. Before doing so, we shall discuss a number of polarimetric parameters that are often encountered in the literature.

3.2 Eigenvalue and Eigenvector-Based Polarimetric Parameters

Cloude (1992) [1] and, later, Cloude and Pottier (1995) [2] introduced a number of polarimetric parameters that are derived from the eigenvalues and eigenvectors that are commonly used today. In this section, we shall discuss

these parameters, as well as others that are commonly encountered in the literature.

3.2.1 Parameters Used to Describe Randomness in Scattering

One such parameter, intended to measure target randomness, is the entropy, which defined as

$$H_T = -\sum_{i=1}^3 P_i \log_3 P_i; \quad P_i = \frac{\lambda_i}{\lambda_1 + \lambda_2 + \lambda_3}. \quad (3.2-1)$$

As pointed out by Cloude [1], the target entropy is a measure of target disorder, with $H_T = 1$ for random targets with three equal eigenvalues and $H_T = 0$ for simple (single, non-random) targets.

Recall from the discussion of polarization responses in Chapter 2 that the amount of variation (that is, randomness) in the scattering properties manifests itself in the form of a “pedestal” in the polarization response. While we normally refer to the pedestal height in the context of the co-polarized response, Durden et al. (1990) [3] showed that measuring the pedestal height is equivalent to measuring the ratio of the minimum eigenvalue to the maximum eigenvalue; that is

$$\text{Pedestal Height} = \frac{\min(\lambda_1, \lambda_2, \lambda_3)}{\max(\lambda_1, \lambda_2, \lambda_3)}. \quad (3.2-2)$$

In reality, this ratio over-estimates the total variation in the observed radar cross-section as a function of polarization. The reason for this is that in order for this minimum and maximum to be realized, both eigenvectors corresponding to those eigenvalues must be valid antenna vectors (see (Eq. 3.1-5)). This is not necessarily the case, possibly resulting in a smaller ratio. Nevertheless, this definition of the pedestal height is a useful measure of the randomness of the scattering process.

Using the model of randomly oriented thin cylinders (we will discuss this in more detail later), Kim and van Zyl (2001) [4] introduced the so-called radar thin vegetation index (RVI):

$$RVI = \frac{4 \min(\lambda_1, \lambda_2, \lambda_3)}{\lambda_1 + \lambda_2 + \lambda_3} = \frac{8\sigma_{hv}}{\sigma_{hh} + \sigma_{vv} + 2\sigma_{hv}}. \quad (3.2-3)$$

(The equation of the right is true for media with reflection symmetry.) This parameter, which is also a measure of the randomness in the scattering, generally varies between 0 and 1. This ratio decreases as the cylinders become

thick compared the radar wavelength. In the limiting case where the cylinders are very thick compared to the radar wavelength, this ratio approaches zero. The factor 4 in Eq. (3.2-3) is arbitrary: it was chosen so that the RVI for a cloud of randomly oriented thin cylinders would be equal to 1.

To illustrate the similarity between these parameters with real image data, we shall first consider the image of San Francisco we discussed in Chapter 2. From the signatures shown in Fig. 2-22, we expect little randomness for the ocean scattering, and significant randomness for the vegetation scattering in the Golden Gate Park area. The urban area should show intermediate randomness. Figure 3-1 shows the comparison of the three measures of randomness introduced above. What is immediately obvious is that these three images convey the same basic information. The only real difference is the scaling from the bare ocean surface to the vegetated areas. The entropy image shows a more compressed scale with less variation in color than the other two. The pedestal height image based on the ratio of the eigenvalues shows the largest dynamic range. Overall, however, there is little reason to prefer one display over the other.

Note how both the entropy and the thin vegetation index show an increase in randomness in the ocean from left to right in the image. Recall that the radar illumination is from the left and that the angle of incidence increases from left to right. The observed increase in randomness in the ocean is due to the decrease in signal-to-noise ratio as the angle of incidence increases. Also, note that not all urban areas show the same amount of randomness. This can be

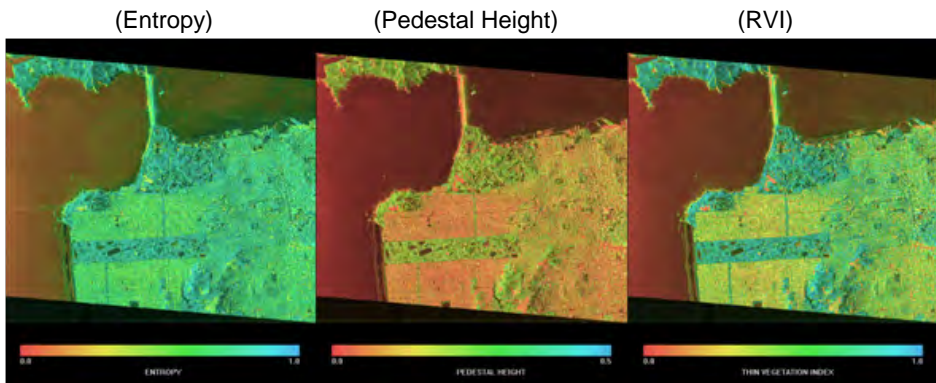


Fig. 3-1. L-band randomness images of San Francisco acquired with the NASA/JPL AIRSAR system. The Golden Gate Bridge is visible in the top center of the image linking the Presidio of San Francisco to the Golden Gate National Recreational Area north of the entrance to San Francisco Bay. Golden Gate Park is the rectangular feature in the lower half of the image in the left portion of the city. The image on the left shows the entropy scaled from 0 to 1. The middle image shows the pedestal height scaled from 0 to 0.5. The image on the right shows the RVI scaled from 0 to 1.

explained by the orientation of the buildings relative to the radar look direction. If a building is oriented such that it presents a large face to the radar, in general, the dominant scattering mechanism is a double reflection off the street onto the face of the building and back to the radar. This is the case above and below Golden Gate Park in the image. If the building is turned slightly, however, such that the front face of the building no longer is orthogonal to the direction in which the radar waves propagate, this double reflection signal no longer travels back to the radar. The result is that other direct reflections from the street and, possibly, the roofs of the buildings begin to dominate, and the signals appear more random. This effect is visible in the middle right portion of the image.

As a second example, we consider an image of a portion of the Black Forest in Germany acquired with the NASA/JPL AIRSAR system during the summer of 1991. The L-band image is shown for reference in Fig. 3-2. The bright feature in the left portion of the image is the town of Villingen. The brighter right-hand portion of the image is a mixed forest consisting of spruce (*Picea abies*), pine (*Pinus sylvestris*), and fir (*Abies alba*) trees. The dry weight biomass ranges up to 50 kilograms per square meter (kg/m^2). The darker areas in the upper portion

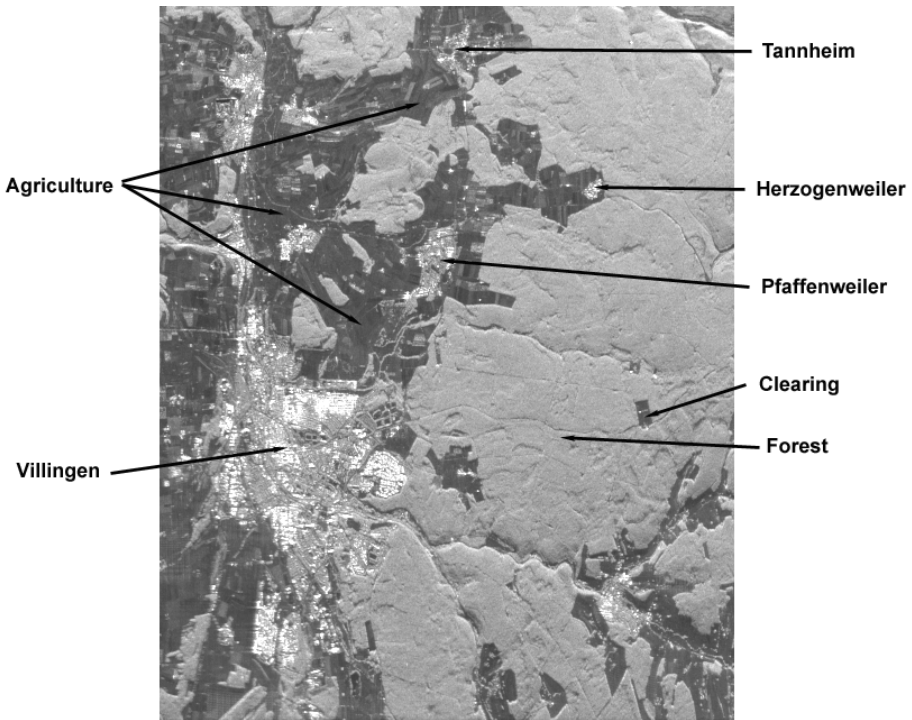


Fig. 3-2. L-band total power image of a portion of the Black Forest in Germany acquired with the NASA/JPL AIRSAR system in the summer of 1991.

and to the left in the image are mostly agricultural fields with varying amounts of biomass, depending on the crop type and maturity of the plants.

Figure 3-3 shows the three parameters calculated from the L-band data. In all cases, the forested areas show significant randomness, and the urban areas show little randomness. The agricultural areas show variations consistent with the amount of vegetation present on a field scale.

Figure 3-4 compares the radar vegetation index for the three frequencies (C-band, L-band, and P-band) that the AIRSAR system uses to acquire images. The C-band images shows much more detail in the agricultural areas because the shorter wavelength is more sensitive to the smaller biomass in these fields. The P-band image, on the other hand, shows a large variation in the forested area. This is due to the increased penetration through the canopy at the longer wavelength with a resulting increase in double reflections from the ground to the trunks of the trees and back to the radar. The variation in RVI is due to the effect that the underlying topography has on the resulting mixture of scattering mechanisms, as discussed by van Zyl (1993) [5].

3.2.2 Alpha Angle

Cloude and Pottier (1996) [6] proposed the following description for the eigenvectors of the covariance matrix:

$$\tilde{\mathbf{e}} = \begin{pmatrix} \cos \alpha & \sin \alpha \cos \beta e^{i\delta} & \sin \alpha \sin \beta e^{i\gamma} \end{pmatrix} \quad (3.2-4)$$

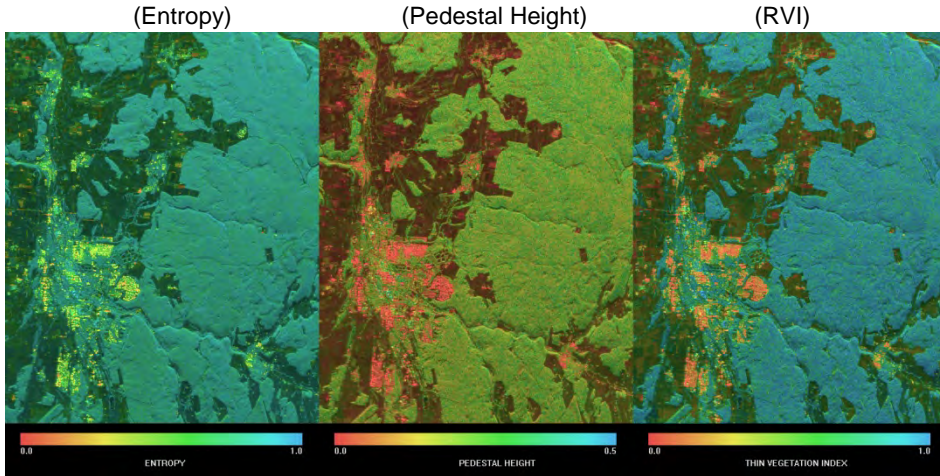


Fig. 3-3. L-band randomness images of the area shown in Fig. 3-2. Forested areas show the highest amount of randomness.

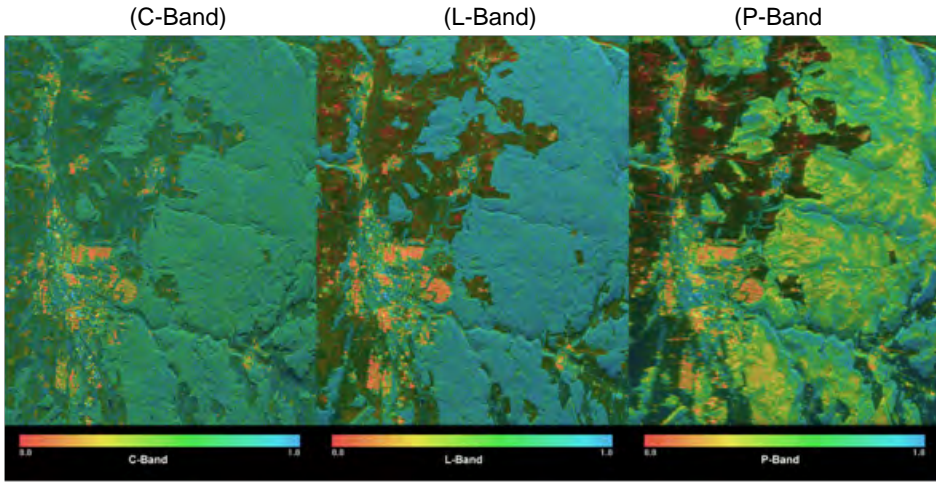


Fig. 3-4. Radar vegetation index images of the area shown in Fig. 3-2 for different frequencies. See the text for a discussion of the images.

in a basis formed by the Pauli matrices. The average angles are then calculated using

$$\bar{\alpha} = \sum_{i=1}^3 \alpha_i P_i, \tag{3.2-5}$$

where P_i is defined in Eq. (3.2-1). The α angle in particular has received significant attention, and, together with the entropy, has been proposed as a way to perform an unsupervised classification of polarimetric SAR images. To investigate the meaning of these angles a bit further, consider that the normalized eigenvector (expressed in Pauli basis) can be written as follows

$$\tilde{\mathbf{e}} = \frac{e^{i\varphi}}{\sqrt{2}(q_{hh} + q_{vv} + 2q_{hv})} \begin{pmatrix} (S_{hh} + S_{vv}) & (S_{hh} - S_{vv})e^{-i\delta} & 2S_{hv}e^{-i\gamma} \end{pmatrix}, \tag{3.2-6}$$

where $q_{xy} = S_{xy}S_{xy}^*$ and the phase angle φ represents the phase of $S_{hh} + S_{vv}$. A comparison of Eq. (3.2-6) and Eq. (3.2-4) now shows that the angle δ is the relative phase between $S_{hh} - S_{vv}$ and $S_{hh} + S_{vv}$. Similarly, the angle γ is the relative phase between S_{hv} and $S_{hh} + S_{vv}$. Next, notice that

$$\tan \beta = \frac{2|S_{hv}|}{|S_{hh} - S_{vv}|} = \frac{2|S_{hv}/S_{vv}|}{|1 - S_{hh}/S_{vv}|} = \frac{2|R_x|}{|1 - R_{co}|}. \tag{3.2-7}$$

The angle β is, therefore, a function of the ratio of the cross-polarized term to the co-polarized VV term in the scattering matrix, as well as the ratio of the two co-polarized terms. The angle α can similarly be written as

$$\tan \alpha = \frac{\sqrt{|1 - R_{co}|^2 + 4|R_x|^2}}{|1 + R_{co}|} \tag{3.2-8}$$

At this point, it is useful to compare these parameters for a few canonical cases. These are summarized in Table 3-1.

The results in Table 3-1 show that the angle α varies from zero deg for trihedral scattering to $\pi/2$ for dihedral scattering. Dipole scattering represents an intermediate case where $\alpha = \pi/4$. Note that this value of α for dipole scattering does not depend on the physical orientation of the dipole. The angle β is near zero for all cases where the cross-polarized return is small compared to the co-polarized returns. For the case of a single dipole, the β angle is related to the physical orientation of the dipole.

Also note that when the cross-polarized term is small compared to the co-polarized ones, the angle α is basically dependent on the co-polarized ratio. For example, in the case of a bare slightly rough surface, this ratio is a function

Table 3-1. Comparison of α and β angles for canonical scatterers.

Scatterer	Matrix Elements	R_{co}	R_x	α	β
Vertical Dipole	$S_{vv} \neq 0; S_{hh} = S_{hv} = 0,$	0	0	$\pi/4$	0
Horizontal Dipole	$S_{hh} \neq 0; S_{vv} = S_{hv} = 0,$	∞	0	$\pi/4$	0
Trihedral	$S_{hh} = S_{vv} = 1, S_{hv} = 0$	1	0	0	0
Dihedral	$S_{hh} = -S_{vv} = 1, S_{hv} = 0$	-1	0	$\pi/2$	0
Dipole oriented at angle ψ w.r.t. horizontal direction	$S_{hh} = \cos^2 \psi$ $S_{vv} = \sin^2 \psi$ $S_{hv} = \sin \psi \cos \psi$	$\tan^2 \psi$	$\tan \psi$	$\pi/4$	2ψ
Slightly Rough Surface	$S_{vv} \geq S_{hh}; R_x \ll 1$	$0 \leq R_{co} \leq 1$	$R_x \ll 1$	$\approx \tan^{-1} \left(\frac{ 1 - R_{co} }{ 1 + R_{co} } \right)$	≈ 0
Dielectric Double Bounce	$S_{vv} \leq S_{hh}; R_x \ll 1$	$0 \geq R_{co} \geq -1$	$R_x \ll 1$	$\approx \tan^{-1} \left(\frac{ 1 - R_{co} }{ 1 + R_{co} } \right)$	≈ 0

of the surface dielectric constant. Therefore, for such a surface, α would be a function of the dielectric constant. For wet surfaces at high incidence angles, dipole scattering. Figure 3-5 shows the alpha angle for different dielectric constants and different incidence angles. Note that as the surface dielectric constant increases, the alpha angle increases as discussed above. Also, because of the change in the co-polarized ratio, as the angle of incidence increases, so does the alpha angle.

In the case of double reflections from dielectric surfaces, the co-polarized ratio will approach infinity at the Brewster angle. For that case, the angle α will also approach $\pi/4$. Figure 3-6 illustrates this point further. The figure illustrates an example where we calculated the alpha angle for a dielectric dihedral reflection assuming that both surfaces have the same dielectric constant. When the dielectric constant becomes very large, the alpha angle approaches $\pi/2$, which is the expected value for a metallic dihedral. For low dielectric constants, however, the alpha angle is closer to 45 deg. Note that for some dielectric constants and angle-of-incidence ranges the alpha angle can actually be less than $\pi/4$. This will mostly happen for low dielectric constant values at larger angles of incidence. These examples illustrate that care must be exercised when interpreting the values of α .

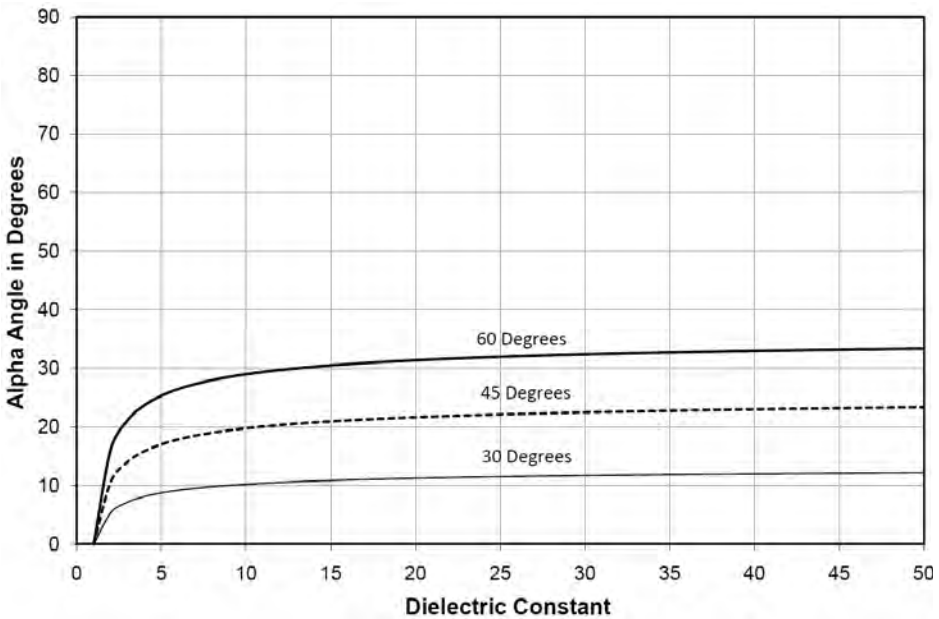


Fig. 3-5. Alpha angle as a function of dielectric constant for a slightly rough dielectric surface for three different incidence angles. Note that as the incidence angle and the dielectric constant increases, the alpha angle also increases. At very large dielectric constants and incidence angles, the alpha angle will approach 45 deg.

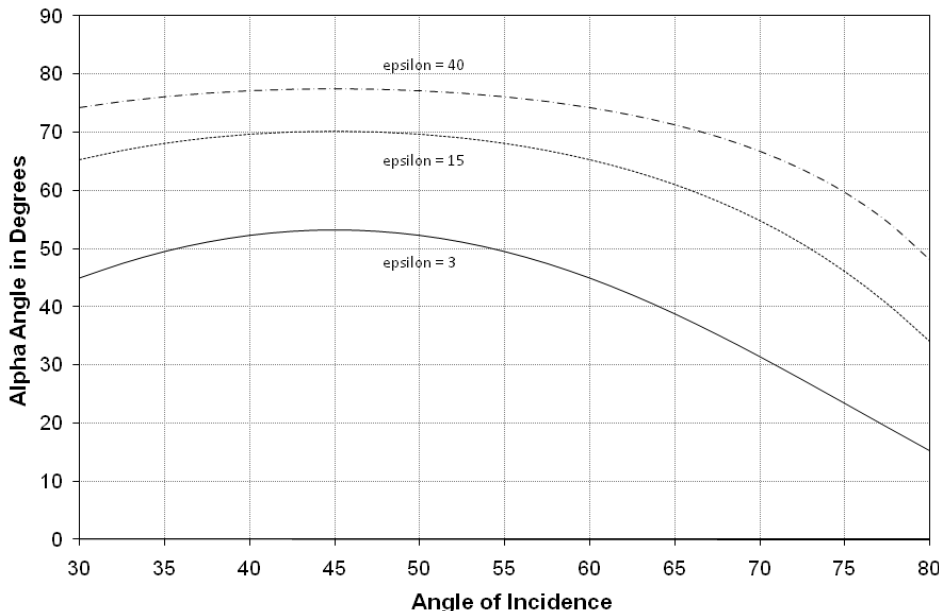


Fig. 3-6. Alpha angle as a function of angle of incidence for a double reflection from two dielectric surfaces with the same dielectric constant (epsilon). At angles of incidence equal to the Brewster angle of the dielectric surfaces, the alpha angle will be 45 deg.

To illustrate the meaning of the alpha angle in image data, Fig. 3.7 shows the L-band alpha angle image for San Francisco. The alpha angle for the ocean is mostly less than 45 deg, consistent with the expectation for a slightly rough surface. Note the increase in the alpha angle with increasing angle of incidence (the angle of incidence increases from left to right across the image) in the ocean, consistent with the predictions shown in Fig. 3-5. The vegetated areas all show alpha angles near 45 deg, consistent with dipole scattering. The urban areas consistently show alpha angles larger than 45 deg, consistent with the expectations for a double-reflection signal from a non-metallic surface.

Figure 3-8 shows the alpha angles at different frequencies for the Black Forest image. As in the case of San Francisco, the urban areas consistently show alpha angles larger than 45 deg. We also see the effect of frequency very clearly in the agricultural areas. At C-band, the alpha angle is mostly near 45 deg, while at L- and P-band, the values are closer to zero, indicating bare (or nearly bare) surfaces. The forested areas at L- and P-band show alpha angles either near 45 deg (especially at L-Band) or larger than 45 deg where there is an appreciable amount of double reflection signal. The C-band image, interestingly, shows the alpha angle in the forested areas to be less than 45 deg and generally less than the values observed in the agricultural areas where there is vegetation. The

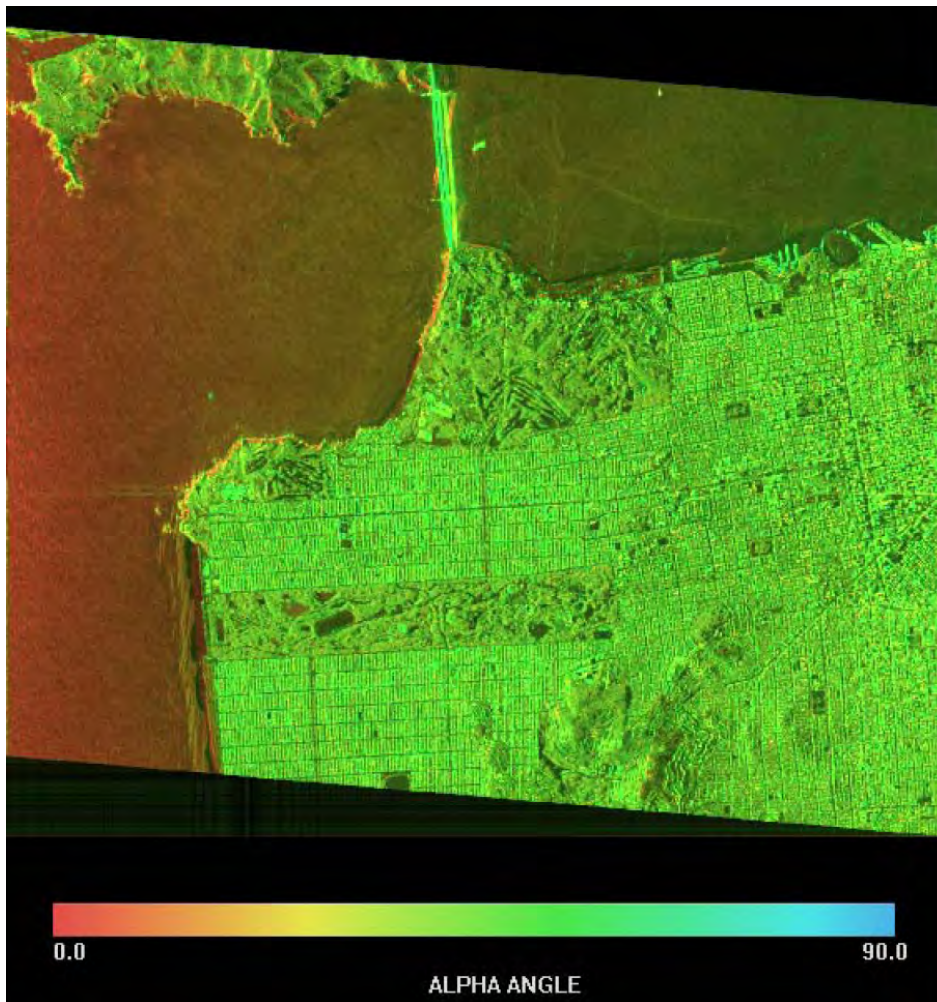


Fig. 3-7. Alpha angle for the San Francisco image. See the text for discussion.

explanation for this lies in the size of the branches relative to the radar wavelength. When we used the term “dipole” before, we could have substituted “cylinder that is thin compared to the radar wavelength.” Let us consider such a cylinder that is oriented vertically. In the thin cylinder limit, we will observe the scattering shown in Table 3-1. As the cylinder becomes thicker compared to the radar wavelength, we observe an increase in the HH term relative to the VV term. In fact, in the thick cylinder limit, the HH term will approach the VV term. As the cylinder radius increase relative to the radar wavelength, therefore, the co-polarized ratio will increase from zero to 1 in the limit of a thick cylinder. Equation (3.2-8) predicts that this will cause the alpha angle to decrease from the 45-deg range as the cylinders increase in thickness relative to

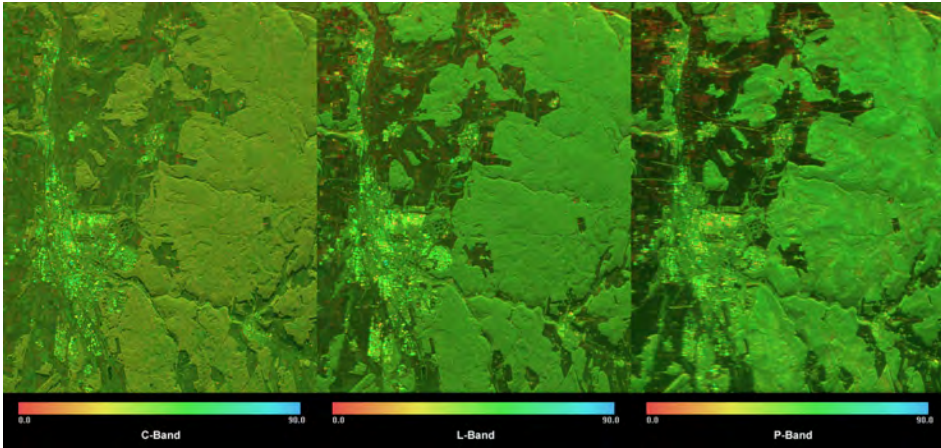


Fig. 3-8. Multi-frequency alpha angle for the Black Forest image. See the text for discussion.

the radar wavelength. In these images, the cylinders are of fixed size, but the radar wavelength changes. At C-band, the radius of a given cylinder will be larger relative to the radar wavelength than at L-band. We would, therefore, expect to see a lower alpha angle at C-band than at L-band.

3.3 Decomposition of Polarimetric Scattering

Earlier in this chapter we discussed the duality between representing a scatterer by its scattering matrix or by an equivalent vector containing the elements of the scattering matrix. In this section, we shall explore this concept in greater detail.

First, let us consider the case of a single scatterer that can be represented by its scattering matrix. We shall further restrict our discussion to the backscatter case where reciprocity is assumed to hold. If we assume that the scattering matrix was measured in the linear basis, we can write

$$\begin{pmatrix} S_{hh} & S_{hv} \\ S_{hv} & S_{vv} \end{pmatrix} = S_{hh} \begin{pmatrix} 1 & 0 \\ 0 & 0 \end{pmatrix} + S_{hv} \begin{pmatrix} 0 & 1 \\ 1 & 0 \end{pmatrix} + S_{vv} \begin{pmatrix} 0 & 0 \\ 0 & 1 \end{pmatrix} \quad (3.3-1)$$

or, in the equivalent vector form,

$$\begin{pmatrix} S_{hh} \\ S_{hv} \\ S_{vv} \end{pmatrix} = S_{hh} \begin{pmatrix} 1 \\ 0 \\ 0 \end{pmatrix} + S_{hv} \begin{pmatrix} 0 \\ 1 \\ 0 \end{pmatrix} + S_{vv} \begin{pmatrix} 0 \\ 0 \\ 1 \end{pmatrix}. \quad (3.3-2)$$

In writing the scattering matrix in vector form, we used an orthogonal basis to express the elements of the scattering vector. It should be immediately obvious

that there are an infinite number of such orthogonal bases that one could choose to represent the scattering vector. Any combination of the form

$$\mathbf{S} = a_1\mathbf{p}_1 + a_2\mathbf{p}_2 + a_3\mathbf{p}_3 \quad (3.3-3)$$

would be permissible as long as

$$\mathbf{p}_i \cdot \mathbf{p}_j = \begin{cases} 0 & \text{if } i \neq j \\ 1 & \text{if } i = j \end{cases} \quad (3.3-4)$$

The logical question is then: Is any basis (other than the one used to make the measurement to begin with) that should be considered for such decomposition? The answer depends on the specific application, but the basis derived from the Pauli spin matrices has a nice intuitive interpretation. This basis is shown in Eq. (3.1-10) in vector form. In matrix form, the basis is

$$\begin{pmatrix} S_{hh} & S_{hv} \\ S_{hv} & S_{vv} \end{pmatrix} = \frac{a}{\sqrt{2}} \begin{pmatrix} 1 & 0 \\ 0 & 1 \end{pmatrix} + \frac{b}{\sqrt{2}} \begin{pmatrix} 1 & 0 \\ 0 & -1 \end{pmatrix} + c \begin{pmatrix} 0 & 1 \\ 1 & 0 \end{pmatrix}. \quad (3.3-5)$$

This decomposition was also used by Krogager (1993) [7] in his thesis. The first two terms involve only the co-polarized elements of the scattering matrix and can be interpreted as scattering by an odd number of reflections from a metallic structure and an even number of reflections from a metallic structure, respectively. The first matrix represents, therefore, scattering from a flat plate, a sphere, or a metallic trihedral corner reflector. The second matrix represent scattering from a metallic dihedral corner reflector.

The third matrix can be interpreted in different ways. Since it only involves the cross-polarized component of the scattering matrix, it is usually interpreted as indicating the amount of random scattering. While this interpretation certainly has some merit in the practical sense that scattering from vegetated areas usually shows a large amount of cross-polarized return, it is not strictly correct from a theoretical point of view. The third matrix, as was pointed out in Chapter 2, is also the scattering matrix of a dihedral corner reflector rotated by 45 deg about the line of sight. The resulting scattered energy is fully polarized, but the polarization vector has been rotated. Admittedly, this is a special case. In most practical applications, a large cross-polarized component is also typically associated with significant depolarization of the scattered energy.

To illustrate the usefulness of this approach for interpreting scattering, we display a color image of San Francisco in Fig. 3-9 in which we assigned the blue color as the magnitude of a in Eq. (3.3-5), the red color as the magnitude of b , and the green color as the magnitude of c . This image shows that the urban area shows a large fraction of the scattering in the red color, which corresponds

to the dihedral component. On the other hand, the ocean shows much more blue on the left, consistent with the single scattering mechanism. The vegetated areas, on the other hand, show significant cross-polarized return. Note the interesting change in color in the ocean from the left to the right in the image, where there is significantly more red visible in the ocean. The explanation for this lies in the fact that for a dielectric surface like the ocean, the co-polarization ratio is a function of both the dielectric constant and the angle of incidence. Figure 3-10 shows the expected co-polarization ratio for a surface with a dielectric constant of 81. The figure also shows the co-polarized ratio to be less than 1, especially at the larger angles of incidence. The Pauli basis, however, forces the HH and VV terms to be equal. Therefore, if the co-polarized ratio is less than 1, a dihedral component is needed to explain the difference between the HH and VV terms.



Fig. 3-9. Color overlay of San Francisco displaying $|S_{hh} + S_{vv}|$ in blue, $|S_{hh} - S_{vv}|$ in red, and $|S_{hv}|$ in green. These three colors are the magnitudes of the scattering matrix elements when they are expressed in the Pauli basis.

The smaller the co-polarization ratio, the stronger the dihedral component required to explain the difference. This is shown as the dashed curve in Fig. 3-10.

It is important to appreciate that the first-order small perturbation model only includes single scattering terms. The fact that the ocean scattering is interpreted to have a significant amount of double reflections occurs only because of the basis under which we have chosen to interpret the scattering. This basis forces the HH and VV components to be the same for the “single scattering” term, leading to this interpretation. This is a fundamental issue with many of the target decomposition schemes proposed in the literature. All of these schemes try to interpret scattering based on an assumption of an underlying basis. If the scattering fits the basis, the interpretation is obviously appropriate. If the basis is not consistent with the actual scattering, however, the interpretation should be modified to take this fact into account. Nevertheless, the Pauli basis provides a good general purpose framework for interpreting polarimetric radar images (as the San Francisco example shows).

Figure 3-11 shows the three-frequency Pauli decompositions for the Black Forest image. These images show a consistent interpretation of the scattering from what we discussed before. The scattering from the randomly oriented

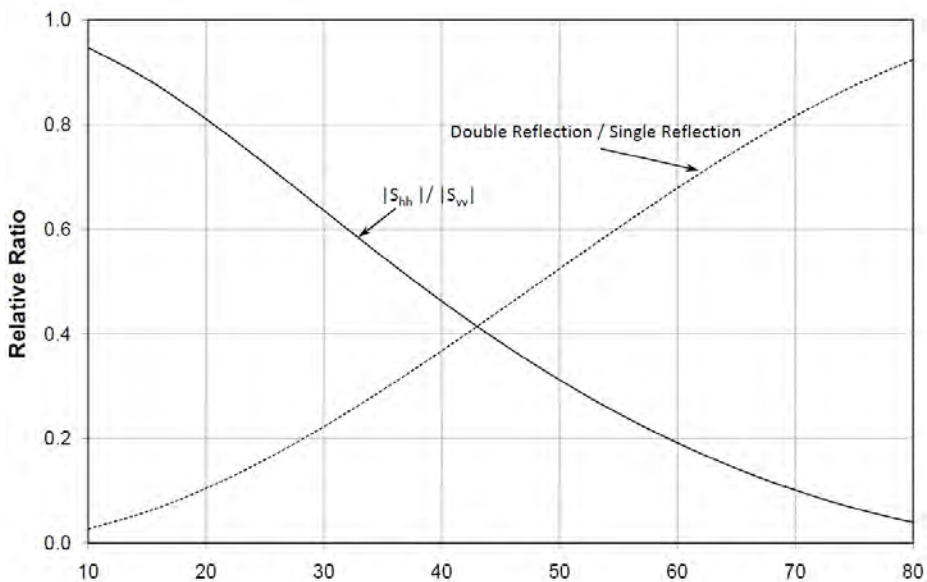


Fig. 3-10. Expected co-polarization ratio and the ratio of double reflection scattering to single reflection scattering as a function of the angle of incidence for a surface with a dielectric constant of 81. The values were calculated using the first-order small perturbation model and assuming the Pauli basis to calculate double and single reflection components.

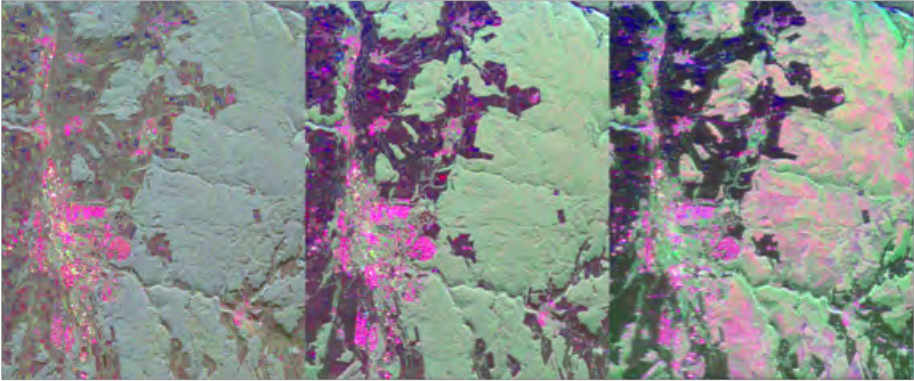


Fig. 3-11. Pauli basis color overlays for the Black Forest image. The color scheme is the same as that in Fig. 3-9. The C-band image is on the left, the L-Band in the middle, and the P-Band on the right.

vegetation is relatively strong in the cross-polarized return. The urban areas, on the other hand, are dominated by dihedral-type reflections at all wavelengths. The increased amount of penetration at P-band shows, relatively speaking, a stronger double reflection signal in much of the forest. The C-band signals interact more with the shorter agricultural crops than the longer wavelengths, resulting in increased cross-polarized returns in those areas.

The discussion so far was concerned with the decomposition of the scattering matrix, or its associated vector form, into orthogonal components. As pointed out before, there is potentially an infinite set of bases we can use for this decomposition. A more important question is the following: What about the case where we have an average covariance matrix? What is the most appropriate way to decompose this observed scattering into simpler parts? We shall discuss this in detail in the next section.

3.3.1 Scattering Decomposition in the Incoherent Case Using Orthonormal Bases

As mentioned in the beginning of this chapter, after multi-looking to reduce speckle, we can write the average covariance matrix as

$$\langle [\mathbf{C}] \rangle = \frac{1}{MN} \sum_{j=1}^M \sum_{i=1}^N [\mathbf{C}]_{ij}, \quad (3.3-6)$$

where the two sums indicate averaging in the range and azimuth directions, respectively. We shall restrict our discussion to the backscatter case, where the individual covariance matrices are defined as

$$[\mathbf{C}] = \begin{pmatrix} S_{hh} \\ \sqrt{2}S_{hv} \\ S_{vv} \end{pmatrix} \begin{pmatrix} S_{hh} & \sqrt{2}S_{hv} & S_{vv} \end{pmatrix}^* = \begin{pmatrix} S_{hh}S_{hh}^* & \sqrt{2}S_{hh}S_{hv}^* & S_{hh}S_{vv}^* \\ \sqrt{2}S_{hv}S_{hh}^* & 2S_{hv}S_{hv}^* & \sqrt{2}S_{hv}S_{vv}^* \\ S_{vv}S_{hh}^* & \sqrt{2}S_{vv}S_{hv}^* & S_{vv}S_{vv}^* \end{pmatrix}. \quad (3.3-7)$$

The covariance matrix is Hermitian. The matrix, therefore, contains, at most, three independent complex numbers and three real numbers, for a total of nine real numbers. The scattering matrix, on the other hand, contains, at most, three complex numbers. If we remove an absolute phase number from one of the elements of the scattering matrix, we would be left with one real and two complex numbers (a total of five real numbers). There must, therefore, be at least four relations between the elements of the covariance matrix of a single scatterer. These are

$$\begin{aligned} C_{00}C_{11} - C_{01}C_{10} &= 2S_{hh}S_{hh}^*S_{hv}S_{hv}^* - \sqrt{2}S_{hh}S_{hv}^*\sqrt{2}S_{hv}S_{hh}^* = 0 \\ C_{00}C_{22} - C_{02}C_{20} &= S_{hh}S_{hh}^*S_{vv}S_{vv}^* - S_{hh}S_{vv}^*S_{vv}S_{hh}^* = 0 \\ C_{11}C_{22} - C_{12}C_{21} &= 2S_{hv}S_{hv}^*S_{vv}S_{vv}^* - \sqrt{2}S_{hv}S_{vv}^*\sqrt{2}S_{vv}S_{hv}^* = 0 \\ C_{00}C_{11}C_{22} - C_{01}C_{02}^*C_{12} &= 2S_{hh}S_{hh}^*S_{hv}S_{hv}^*S_{vv}S_{vv}^* - \sqrt{2}S_{hh}S_{hv}^*S_{vv}S_{hh}^*\sqrt{2}S_{hv}S_{vv}^* = 0 \end{aligned} \quad (3.3-8)$$

Once we perform the averaging process shown in Eq. (3.3-6) during the multi-looking process, these relations will no longer hold. Instead, the equal signs should be replaced with greater than or equal to signs. In fact, that is simply a statement of the Cauchy-Schwarz inequality applied to complex numbers. Therefore, in general,

$$\begin{aligned} C_{00}C_{11} - C_{01}C_{10} &\geq 0 \\ C_{00}C_{22} - C_{02}C_{20} &\geq 0 \\ C_{11}C_{22} - C_{12}C_{21} &\geq 0 \\ C_{00}C_{11}C_{22} - C_{01}C_{02}^*C_{12} &\geq 0 \end{aligned} \quad (3.3-9)$$

Unless equality holds in each of the four cases, we cannot find an equivalent scattering matrix to fully represent the scattering described by the covariance matrix as shown in Eq. (3.3-7). A reasonable question then is whether we can find a set of scattering matrices that, when transformed to their covariance matrices, could be added to fully describe the observed covariance matrix. To answer this question, consider the decomposition proposed by Cloude (1992) [1]:

$$\langle [\mathbf{C}] \rangle = \sum_{i=1}^3 \lambda_i \hat{\mathbf{e}}_i \hat{\mathbf{e}}_i^\dagger. \quad (3.3-10)$$

This decomposition is unique. That is, since the eigenvectors of the covariance matrix are orthogonal, they form a natural basis in which to express the scattering. There is one potential problem with this decomposition. Since the decomposition is performed for each covariance matrix (that is, on a pixel-by-pixel basis in an image), the resulting basis for the decomposition changes from pixel to pixel. This could make it more difficult to compare the meaning of a given eigenvalue in different areas without also looking at the associated eigenvectors that form the basis. To illustrate what we mean, consider the special case of the covariance matrix of terrain with reflection symmetry. In that case, the covariance matrix has the special form (Borgeaud et al., 1985) [8]:

$$\langle [\mathbf{C}] \rangle = \begin{pmatrix} \xi & 0 & \rho \\ 0 & \eta & 0 \\ \rho^* & 0 & \zeta \end{pmatrix}, \quad (3.3-11)$$

where

$$\begin{aligned} \xi &= \langle S_{hh} S_{hh}^* \rangle \\ \rho &= \langle S_{hh} S_{vv}^* \rangle \\ \eta &= 2 \langle S_{hv} S_{hv}^* \rangle \\ \zeta &= \langle S_{vv} S_{vv}^* \rangle \end{aligned} \quad (3.3-12)$$

The parameters ξ, η, ζ and ρ all depend on the size, shape, and electrical properties of the scatterers, as well as their statistical distribution. It is easily shown that the eigenvalues of $\langle [\mathbf{C}] \rangle$ are

$$\begin{aligned} \lambda_1 &= \frac{1}{2} \left\{ \xi + \zeta + \sqrt{(\xi - \zeta)^2 + 4|\rho|^2} \right\} \\ \lambda_2 &= \frac{1}{2} \left\{ \xi + \zeta - \sqrt{(\xi - \zeta)^2 + 4|\rho|^2} \right\}. \\ \lambda_3 &= \eta \end{aligned} \quad (3.3-13)$$

All these are real numbers, as expected for a Hermitian matrix. It follows from inspection that the first and third eigenvalues are positive. To show that the second eigenvalue is also positive, note that, from the second relationship in Eq. (3.3-10),

$$\xi\zeta \geq |\rho|^2 \Rightarrow (\xi - \zeta)^2 + 4|\rho|^2 \leq (\xi + \zeta)^2. \tag{3.3-14}$$

Hence, the second eigenvalue is also positive.

The corresponding three eigenvectors are

$$\begin{aligned} \mathbf{k}_1 &= \sqrt{\frac{[\zeta - \xi + \sqrt{\Delta}]^2}{[\zeta - \xi + \sqrt{\Delta}]^2 + 4|\rho|^2}} \begin{pmatrix} 2\rho/[\zeta - \xi + \sqrt{\Delta}] \\ 0 \\ 1 \end{pmatrix} \\ \mathbf{k}_2 &= \sqrt{\frac{[\zeta - \xi - \sqrt{\Delta}]^2}{[\zeta - \xi - \sqrt{\Delta}]^2 + 4|\rho|^2}} \begin{pmatrix} 2\rho/[\zeta - \xi - \sqrt{\Delta}] \\ 0 \\ 1 \end{pmatrix}. \\ \mathbf{k}_3 &= \begin{pmatrix} 0 \\ 1 \\ 0 \end{pmatrix}. \end{aligned} \tag{3.3-15}$$

In these expressions, we used the shorthand notation

$$\Delta = (\zeta - \xi)^2 + 4|\rho|^2. \tag{3.3-16}$$

We note that Δ is always positive. Also note that we can write the ratio of the first elements of the first two eigenvectors as

$$\frac{k_{11}}{k_{21}} = - \frac{\sqrt{\left\{ [\zeta - \xi + \sqrt{\Delta}]^2 \right\} \left\{ [\zeta - \xi - \sqrt{\Delta}]^2 + 4|\rho|^2 \right\}} [\zeta - \xi - \sqrt{\Delta}]^2}{\sqrt{\left\{ [\zeta - \xi - \sqrt{\Delta}]^2 \right\} \left\{ [\zeta - \xi + \sqrt{\Delta}]^2 + 4|\rho|^2 \right\}} 4|\rho|^2}, \tag{3.3-17}$$

which is always negative. This means that the first two eigenvectors represent scattering matrices that can be interpreted in terms of odd and even numbers of reflections. Without looking explicitly at the eigenvectors, however, we will not know which eigenvalue to associate with which scattering mechanism.

Figure 3-12 illustrates this with an example. On the left, we display the image of San Francisco previously discussed with the three eigenvalues as defined in Eq. (3.3-13) colored blue for the first eigenvalue, red for the second, and green for the third. Note that the third eigenvalue and eigenvector are identical to the third Pauli element encountered before. The ocean is dominated by a blue color, indicating that the scattering is dominated by whatever scattering mechanism

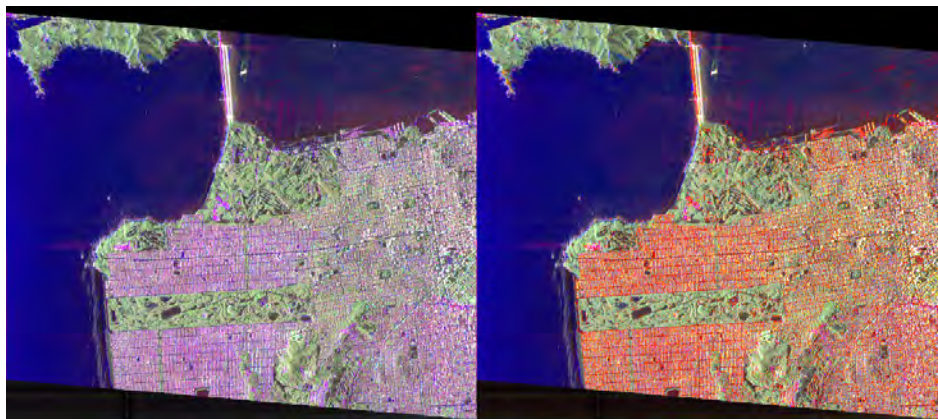


Fig. 3-12. Two color overlays for the image of San Francisco. In the image on the left, colors are assigned to the three eigenvalues without further examining the eigenvectors. The first eigenvalue is colored blue, the second red, and the third green. In the image on the right, the co-polarized phase of the first eigenvector is used to determine the color of the first eigenvalue. If the phase is more consistent with odd numbers of reflections, the eigenvalue is colored blue. Otherwise it is colored red. The color of the second eigenvector is determined using the fact that the two co-polarized phases of the first two eigenvectors are 180 deg different.

the first eigenvector represents. The urban areas, however, are also dominated by a blue color, indicating the same. Vegetated areas consistently show a green color, indicating that depolarization is, relatively speaking, high. On the right panel of Fig. 3-12, we show the same image, but this time we examined the eigenvectors for each pixel. If the co-polarized phase is in the range $[-90^\circ; 90^\circ]$, we assign a blue color to the eigenvalue corresponding to that eigenvector. If the co-polarized phase is in the range $[90^\circ; 270^\circ]$, we assign a red color. We already showed that the phase difference between the first two eigenvectors is 180 deg; once we identified the color for the first eigenvector, therefore, the color for the second is automatically determined. This image on the right is quite different from the one on the left. In particular, the urban area in the image on the right is now dominated by red, indicating scattering more consistent with double reflections.

Comparing the results on the right in Fig. 3-12 with those in Fig. 3-9, we note many similarities between the Pauli basis display and the eigenvalue display. The main difference is that the eigenvalue display colors appear more pure. Also, note that the gradient from blue to red in the ocean is not as pronounced in the image on the right in Fig. 3-12. The reason is that while the Pauli basis insists that the co-polarized terms have the same amplitude, the eigenvectors do not (see Eq. (3.3-15)).

A natural question is then: Is there a preferred basis in which to do the decomposition? In general, we could also choose to write the average covariance matrix in the following form

$$\langle [\mathbf{C}] \rangle = \sum_{i=1}^3 w_i \mathbf{p}_i \mathbf{p}_i^\dagger \quad (3.3-18)$$

$$\mathbf{p}_i \mathbf{p}_j^\dagger = \begin{cases} 1 & \text{if } i = j \\ 0 & \text{if } i \neq j \end{cases}.$$

The Pauli and the eigenvalue bases are two special cases of this decomposition. The answer to this question is not obvious. It depends largely on the goal of the analysis. As our discussion shows, the decomposition is not the hard part; interpreting the results is. This desire to be able to interpret the results of such decomposition is what led many researchers to propose decompositions based on specific models, rather than orthogonal bases as discussed so far. We shall look at this in more detail in the next section.

3.3.2 Model Based Scattering Decomposition in the Incoherent Case

The basic idea behind model-based decompositions is to hypothesize that the measured covariance matrix can be modeled as the combination of a number of individual matrices representing scattering as predicted by models. In this section we shall examine a number of different model-based decomposition schemes in more detail.

3.3.2.1 Freeman-Durden Three-Component Scattering Decomposition. For vegetated terrain, we could hypothesize that the dominant scattering mechanisms might be direct scattering from randomly oriented branches, plus double reflections from the ground/trunk combination, plus direct (although attenuated) scattering from the underlying ground surface. This is the basic idea behind the three-component scattering decomposition proposed by Freeman and Durden (1998) [9]. This decomposition can be written as follows

$$\langle [\mathbf{C}] \rangle = f_s [\mathbf{C}_{ground}] + f_d [\mathbf{C}_{trunk-ground}] + f_v [\mathbf{C}_{branches}], \quad (3.3-19)$$

with

$$\begin{aligned}
 [\mathbf{C}_{ground}] &= \begin{pmatrix} |\beta|^2 & 0 & \beta \\ 0 & 0 & 0 \\ \beta^* & 0 & 1 \end{pmatrix} \\
 [\mathbf{C}_{trunk-ground}] &= \begin{pmatrix} |\alpha|^2 & 0 & \alpha \\ 0 & 0 & 0 \\ \alpha^* & 0 & 1 \end{pmatrix} . \\
 \langle [\mathbf{C}_{branches}] \rangle &= \begin{pmatrix} 1 & 0 & 1/3 \\ 0 & 2/3 & 0 \\ 1/3 & 0 & 1 \end{pmatrix}
 \end{aligned} \tag{3.3-20}$$

The matrix representing branch scattering assumes that the branches are thin compared to the radar wavelength and that the branches are uniformly randomly oriented. We previously discussed this case in Chapter 2. From Eq. (3.3-19) one can then derive the following four equations:

$$\begin{aligned}
 \langle |S_{hh}|^2 \rangle &= f_s |\beta|^2 + f_d |\alpha|^2 + f_v \\
 \langle |S_{vv}|^2 \rangle &= f_s + f_d + f_v \\
 \langle |S_{hv}|^2 \rangle &= f_v/3 \\
 \langle |S_{hh}S_{vv}^*| \rangle &= f_s \beta + f_d \alpha + f_v/3
 \end{aligned} \tag{3.3-21}$$

Freeman and Durden (1998) [9] point out that there are four equations and five unknowns. They then make the following crucial suggestion: since neither the ground reflection nor the double reflection terms add to the predicted cross-polarized return, they can use the measured cross-polarized return to solve for the parameter f_v . They continue to suggest that the volume contribution can then be subtracted from the measured matrix before solving for the other terms. In other words, we can write Eq. (3.3-19) as

$$\langle [\mathbf{C}] \rangle - \begin{pmatrix} 3\langle |S_{hv}|^2 \rangle & 0 & \langle |S_{hv}|^2 \rangle \\ 0 & 2\langle |S_{hv}|^2 \rangle & 0 \\ \langle |S_{hv}|^2 \rangle & 0 & 3\langle |S_{hv}|^2 \rangle \end{pmatrix} = f_s [\mathbf{C}_{ground}] + f_d [\mathbf{C}_{trunk-ground}] \tag{3.3-22}$$

Once the subtraction has been done, there are three remaining equations in four unknowns, as follows:

$$\begin{aligned} \langle |S_{hh}|^2 \rangle' &= f_s |\beta|^2 + f_d |\alpha|^2 \\ \langle |S_{vv}|^2 \rangle' &= f_s + f_d \\ \langle |S_{hh} S_{vv}^*| \rangle' &= f_s \beta + f_d \alpha \end{aligned} \quad (3.3-23)$$

The primes on the left serve to remind us that these are the quantities after the volume-scattering contribution have been subtracted. The phase of the remaining co-polarized component is then used to fix either α or β . The argument is that if the residual co-polarized phase is closer to zero than to π , surface scattering dominates and we should solve for β explicitly. Therefore, we set $\alpha = -1$ (indicating a double reflection) and solve for the remaining parameters. On the other hand, if the residual co-polarized phase is closer to π than to zero, double reflection scattering dominates and we should solve for α explicitly. In this case, we set $\beta = 1$ (indicating a single reflection) and solve for the remaining parameters.

Figure 3-13 shows a color overlay image of the three contributions calculated using the Freeman and Durden (1998) [9] model for the image of the Black Forest at L-band. The image on the left shows the relative strength of the three scattering mechanisms in the color code indicated. Overall, the image clearly shows volume scattering to dominate in the vegetated areas, double reflections to dominate in the urban areas, and some of the agricultural areas to show surface scattering. At this qualitative level, the results appear consistent with our expectations. The image is also similar to the Pauli basis image shown in the middle of Fig. 3-11.

However, a deeper examination shows a significant flaw in this decomposition. The image on the right shows the results of an analysis of the eigenvalues of the matrix on the left in Eq. (3.3-22) after we subtracted the vegetation contribution from the original data. If any of the eigenvalues are negative, we blanked out the pixel in the image on the right in Fig. 3-13. This surprising result shows that the majority of the pixels in the vegetated area end up with negative eigenvalues after we subtracted the scattering from the vegetation, as suggested by Freeman and Durden (1998) [9]. However, this is exactly where we expect the scattering model for scattering from the vegetation to be most applicable! We shall show later that this surprising result is the consequence of assigning all the cross-polarized return to the vegetation scattering.

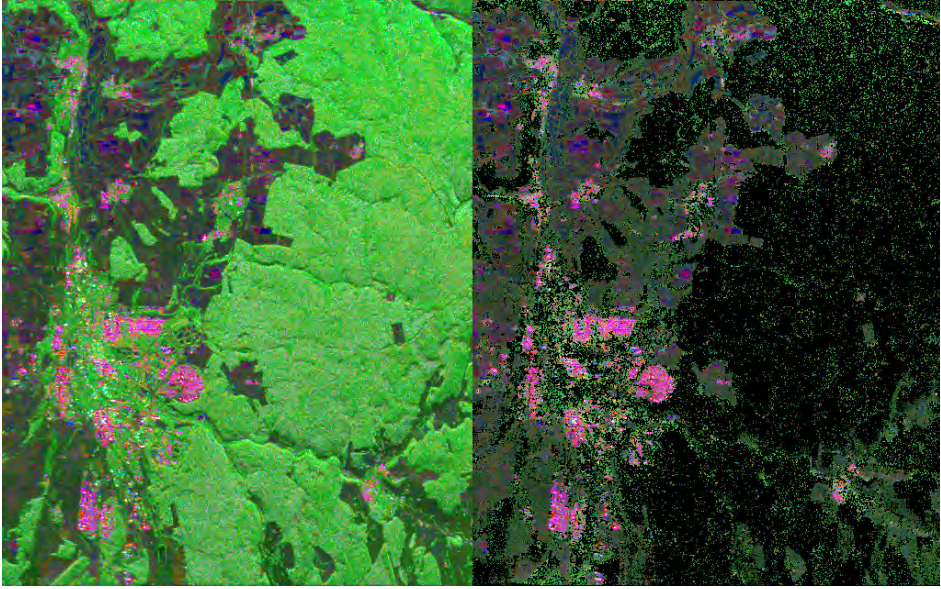


Fig. 3-13. Two color overlays displaying the results of the Freeman and Durden decomposition applied to the L-band image of the Black Forest. The image on the left displays the surface contribution in blue, the double reflection contribution in red, and the vegetation contribution in green. The image on the right shows only those pixels with non-negative eigenvalues once the vegetation contribution has been subtracted. See the text for more discussion.

3.3.2.2 Four-Component Model Proposed by Yamaguchi et al. The three-component model described above assumes that the terrain has reflection symmetry by ignoring the terms in the covariance matrix that involves products of co-polarized and cross-polarized terms. While this assumption seems to be valid for most types of terrain in the sense that these components of the covariance matrix are much smaller than the others, one cannot always assume that reflection symmetry will hold. Yamaguchi et al. (2005) [10] recognized this fact and proposed an extension of the three-component model to include a term that would account for the non-zero products of co-polarized and cross-polarized terms. Their decomposition is written as

$$\langle [C] \rangle = f_s [C_{ground}] + f_d [C_{trunk-ground}] + f_v [C_{branches}] + f_c [C_{helix}], \quad (3.3-24)$$

with the matrix representing the helix scattering taking one of the following two forms:

$$[C_{r-helix}] = \frac{1}{4} \begin{pmatrix} 1 & j\sqrt{2} & -1 \\ -j\sqrt{2} & 2 & j\sqrt{2} \\ -1 & -j\sqrt{2} & 1 \end{pmatrix}; \quad [C_{l-helix}] = \frac{1}{4} \begin{pmatrix} 1 & -j\sqrt{2} & -1 \\ j\sqrt{2} & 2 & -j\sqrt{2} \\ -1 & j\sqrt{2} & 1 \end{pmatrix}. \quad (3.3-25)$$

Note that these two matrices both predict the cross products $\langle S_{hh}S_{hv}^* \rangle$ and $\langle S_{hv}S_{vv}^* \rangle$ to be purely imaginary numbers. This might not be the case in observed data. To get around this, Yamaguchi et al. (2005) [10] recommend using only the imaginary portion of the observed cross-products in the decomposition. Furthermore, the model matrices predict that $\langle S_{hh}S_{hv}^* \rangle = \langle S_{hv}S_{vv}^* \rangle$. Again, this might not be exactly what is observed. Therefore, they recommend using

$$\frac{f_c}{4} = \frac{1}{2} \left| \text{Im} \left\{ \langle S_{hh}S_{hv}^* \rangle + \langle S_{hv}S_{vv}^* \rangle \right\} \right| \quad (3.3-26)$$

Finally, to decide which matrix in Eq. (3.3-25) to use, they propose

$$\text{if } \begin{cases} \text{Im} \left\{ \langle S_{hh}S_{hv}^* \rangle + \langle S_{hv}S_{vv}^* \rangle \right\} > 0 & \Rightarrow \text{ use } [\mathbf{C}_{r\text{-helix}}] \\ \text{Im} \left\{ \langle S_{hh}S_{hv}^* \rangle + \langle S_{hv}S_{vv}^* \rangle \right\} < 0 & \Rightarrow \text{ use } [\mathbf{C}_{l\text{-helix}}] \end{cases} \quad (3.3-27)$$

Assuming a uniformly oriented canopy, and writing out the covariance matrices in Eq. (3.3-24), we find the following five equations with six unknowns:

$$\begin{aligned} \langle |S_{hh}|^2 \rangle &= f_s |\beta|^2 + f_d |\alpha|^2 + \frac{3}{8} f_v + \frac{1}{4} f_c \\ \langle |S_{hv}|^2 \rangle &= \frac{1}{8} f_v + \frac{1}{4} f_c \\ \langle |S_{vv}|^2 \rangle &= f_s + f_d + \frac{3}{8} f_v + \frac{1}{4} f_c \\ \langle S_{hh}S_{vv}^* \rangle &= f_s \beta + f_d \alpha + \frac{1}{8} f_v - \frac{1}{4} f_c \\ \frac{1}{2} \left| \text{Im} \left\{ \langle S_{hh}S_{hv}^* \rangle + \langle S_{hv}S_{vv}^* \rangle \right\} \right| &= \frac{f_c}{4} \end{aligned} \quad (3.3-28)$$

The unknown quantities are $\alpha, \beta, f_s, f_d, f_v$ and f_c . To solve for these unknowns, note that the last expression allows us to find f_c as follows

$$f_c = 2 \left| \text{Im} \left\{ \langle S_{hh}S_{hv}^* \rangle + \langle S_{hv}S_{vv}^* \rangle \right\} \right| \quad (3.3-29)$$

We can then use the second equation in Eq. (3.3-28) to find f_v , as follows:

$$f_v = 8 \left(\left\langle |S_{hv}|^2 \right\rangle - \frac{f_c}{4} \right). \quad (3.3-30)$$

Once these two unknowns are determined, the contributions of the helix scattering and the volume scattering can be subtracted from the observed covariance matrix. Solving for the remaining unknowns then follows the same procedure as outlined by Freeman and Durden (1998) [9] as discussed in the previous section. Specifically,

$$f_s [\mathbf{C}_{ground}] + f_d [\mathbf{C}_{trunk-ground}] = \langle [\mathbf{C}] \rangle - \frac{f_v}{8} \begin{pmatrix} 3 & 0 & 1 \\ 0 & 2 & 0 \\ 1 & 0 & 3 \end{pmatrix} - \frac{f_c}{4} \begin{pmatrix} 1 & \pm j\sqrt{2} & -1 \\ \mp j\sqrt{2} & 2 & \pm j\sqrt{2} \\ -1 & \mp j\sqrt{2} & 1 \end{pmatrix}. \quad (3.3-31)$$

Yamaguchi et al. (2005) [10] went one step further than the Freeman and Durden (1998) [9] decomposition in that they recognized that not all vegetated terrains are well represented by a uniformly oriented canopy. In some cases, the orientations are preferentially vertical, while in others it might be preferentially horizontal. For these cases, Yamaguchi et al. [10] propose to use cosine-squared distributions around either vertical or horizontal directions, which leads to the following covariance matrices

$$[\mathbf{C}_{branches_h}] = \frac{1}{15} \begin{pmatrix} 8 & 0 & 2 \\ 0 & 4 & 0 \\ 2 & 0 & 3 \end{pmatrix}; \quad [\mathbf{C}_{branches_v}] = \frac{1}{15} \begin{pmatrix} 3 & 0 & 2 \\ 0 & 4 & 0 \\ 2 & 0 & 8 \end{pmatrix}. \quad (3.3-32)$$

In their decomposition algorithm, Yamaguchi et al. [10] use the ratio of the VV to HH cross-sections to decide which canopy model to use. If the ratio of VV to HH power is less than -2 dB, they use the cosine-squared distribution around the horizontal direction. If the ratio is between -2 dB and +2 dB, they use the uniform distribution. When the ratio is larger than +2 dB, they use the cosine-squared distribution around the vertical direction. In the case where we use a distribution that is preferentially horizontal, the expressions in Eq. (3.3-28) need to be modified as follows:

$$\begin{aligned}
\langle |S_{hh}|^2 \rangle &= f_s |\beta|^2 + f_d |\alpha|^2 + \frac{8}{15} f_v + \frac{1}{4} f_c \\
\langle |S_{hv}|^2 \rangle &= \frac{2}{15} f_v + \frac{1}{4} f_c \\
\langle |S_{vv}|^2 \rangle &= f_s + f_d + \frac{3}{8} f_v + \frac{1}{4} f_c \\
\langle S_{hh} S_{vv}^* \rangle &= f_s \beta + f_d \alpha + \frac{3}{15} f_v - \frac{1}{4} f_c \\
\frac{1}{2} \left| \text{Im} \left\{ \langle S_{hh} S_{hv}^* \rangle + \langle S_{hv} S_{vv}^* \rangle \right\} \right| &= \frac{f_c}{4}
\end{aligned} \quad (3.3-33)$$

The helix component is still determined by Eq. (3.3-29), but we now have to modify how we determine the volume component, as follows:

$$f_v = \frac{15}{2} \left(\langle |S_{hv}|^2 \rangle - \frac{f_c}{4} \right). \quad (3.3-34)$$

The surface and double reflection components are then determined using the Freeman and Durden (1998) [9] approach after the following subtraction

$$f_s [\mathbf{C}_{ground}] + f_d [\mathbf{C}_{trunk-ground}] = \langle [\mathbf{C}] \rangle - \frac{f_v}{15} \begin{pmatrix} 8 & 0 & 2 \\ 0 & 4 & 0 \\ 2 & 0 & 3 \end{pmatrix} - \frac{f_c}{4} \begin{pmatrix} 1 & \pm j\sqrt{2} & -1 \\ \mp j\sqrt{2} & 2 & \pm j\sqrt{2} \\ -1 & \mp j\sqrt{2} & 1 \end{pmatrix}. \quad (3.3-35)$$

In the case where the ratio of VV to HH is larger than +2 dB, we assume a preferentially vertical orientation, the helix component is determined as before, and the volume component is determined by Eq. (3.3-34). The surface and double reflection components are determined after the following subtraction

$$f_s [\mathbf{C}_{ground}] + f_d [\mathbf{C}_{trunk-ground}] = \langle [\mathbf{C}] \rangle - \frac{f_v}{15} \begin{pmatrix} 3 & 0 & 2 \\ 0 & 4 & 0 \\ 2 & 0 & 8 \end{pmatrix} - \frac{f_c}{4} \begin{pmatrix} 1 & \pm j\sqrt{2} & -1 \\ \mp j\sqrt{2} & 2 & \pm j\sqrt{2} \\ -1 & \mp j\sqrt{2} & 1 \end{pmatrix}. \quad (3.3-36)$$

The Yamaguchi et al. (2005) [10] algorithm can be summarized as follows:

- 1) Estimate the helix scattering component using Eq. (3.3-29).
- 2) Depending on the ratio of VV to HH, use Eq. (3.3-30) ($-2 \text{ dB} < \text{VV/HH} < 2 \text{ dB}$) or Eq. (3.3-34) ($\text{VV/HH} < -2 \text{ dB}$ or $\text{VV/HH} > +2 \text{ dB}$) to estimate the volume component.

- 3) Subtract the helix and volume components from the observation using Eq. (3.3-31) when $-2 \text{ dB} < \text{VV/HH} < 2 \text{ dB}$, Eq. (3.3-35) when $\text{VV/HH} < -2 \text{ dB}$ or Eq. (3.3-35) when $\text{VV/HH} > +2 \text{ dB}$.
- 4) Use Eq. (3.3-23) and the process described by Freeman and Durden (1998) [9] to estimate the strength of the surface and double reflection scattering terms.

Figure 3-14 shows the results of applying the Yamaguchi et al. (2005) [10] decomposition to the L-band image of the Black Forest. The image on the left shows the relative strength of the volume, double bounce, and surface scattering with the same color scheme that we used for the Freeman and Durden (1998) [9] decomposition in Fig. 3-13. Also shown in the figure on the right are the pixels with negative eigenvalues after the helix and volume components have been subtracted. Comparing Fig. 3-14 and Fig. 3-13, we note that the qualitative results of the decompositions are very similar. This is not surprising, since the helix components are typically much smaller than the others. The major difference between the two decomposition methods lies in the number of pixels with negative eigenvalues. The Yamaguchi et al. (2005) [10] decomposition results show significantly fewer pixels with negative eigenvalues. It should be pointed out that Yamaguchi et al. (2005) [10]

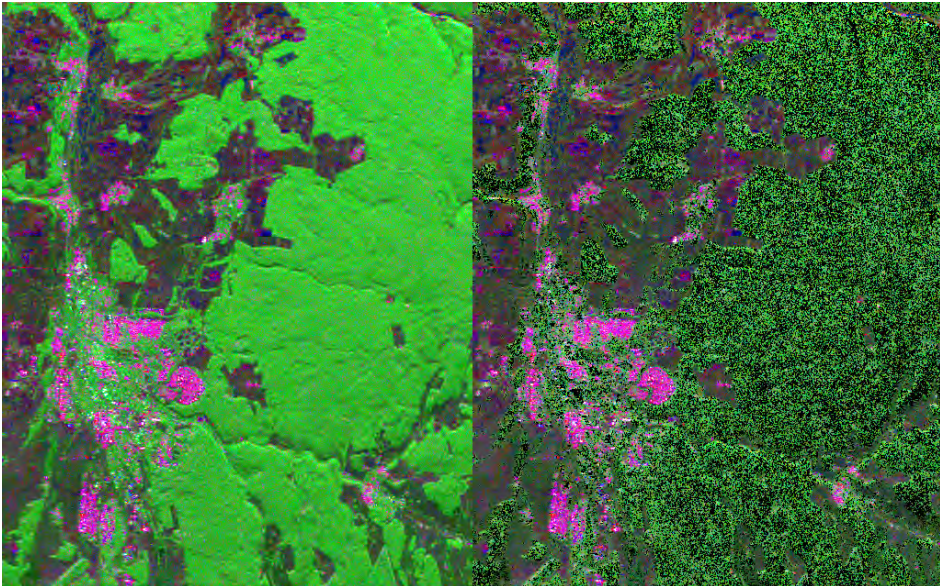


Fig. 3-14. Two color overlays displaying the results of the Yamaguchi et al. [10] decomposition applied to the L-band image of the Black Forest. The image on the left displays the surface contribution in blue, the double reflection contribution in red, and the vegetation contribution in green. The image on the right shows only those pixels with non-negative eigenvalues once the vegetation contribution has been subtracted. See the text for more discussion.

recognized that areas where the HV returns exceed approximately half that of HH or VV could lead to negative powers in the decomposition. Their solution was to apply a slightly different algorithm to pixels that show this high relative value of HV. In the next section we shall describe a systematic way of determining the level of the volume scattering while still ensuring that no negative powers will result.

Figure 3-15 shows the relative strength of the helix term in the Yamaguchi et al. [10] decomposition. Notice that the helix terms are stronger in the vegetated areas, but overall still relatively small, rarely exceeding 10 percent of the scattering. The image in the right shows the strength of the helix term when it is not normalized by the total power. It is interesting to note that the areas indicated by the arrows show modulations that appear to be consistent with the along-track slopes caused by the local topography. This image was analyzed by van Zyl (1993) [5] who showed that the scattering mechanisms at P-band are strongly modulated by the topographic slopes in the range direction. The fact that the strength of the helix term might be influenced by the along-track slopes should not be a surprise because it is well known that along-track tilts lead to

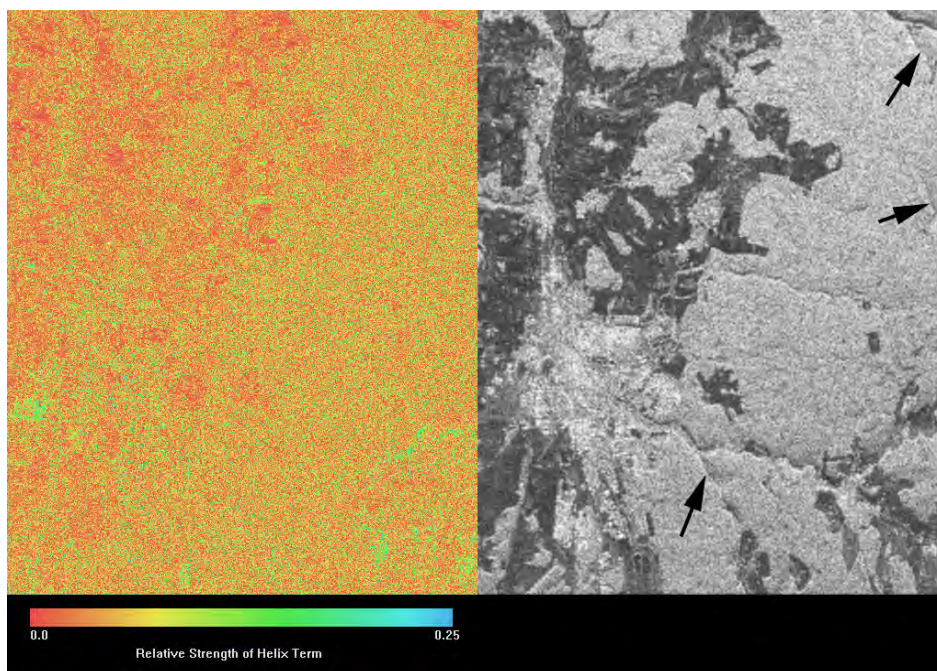


Fig. 3-15. The image on the left displays the relative strength of the helix term in the Yamaguchi et al. [10] decomposition as a fraction of the total power. While the helix term is slightly stronger in the vegetated areas, it is relatively small compared to the overall scattering. The image on the right shows the strength of the helix term when it is not normalized. The arrows indicate areas where the strength of the helix term is modulated by the topographic slopes in the along-track direction. Images were calculated at L-band.

non-zero correlations between co- and cross-polarized components of the scattering matrix (Shuler et al., 1996 [11]; Lee et al., 2000 [12]), even for terrains that otherwise would exhibit reflection symmetry.

To better understand how azimuth slopes affect the co- and cross-polarized correlation, consider the analysis shown in Appendix A for a tilted surface. We show that the scattering matrix of the tilted surface $[\mathbf{S}(\theta)]$ can be written as a transformation of the scattering matrix of the surface without tilts $[\mathbf{S}_l(\theta_l)]$, as follows

$$\mathbf{S}(\theta) = [\tilde{\mathbf{T}}_R] \mathbf{S}_l(\theta_l) [\mathbf{T}_R]. \quad (3.3-37)$$

The angles refer to the angle of incidence in either the global coordinate system (θ) or the local coordinate system (θ_l) for the surface. For details, please see the appendix. The transformation matrix takes the form of a coordinate rotation

$$[\mathbf{T}_R] = \begin{pmatrix} \cos \varphi & \sin \varphi \\ -\sin \varphi & \cos \varphi \end{pmatrix}; \quad \tan \varphi = \frac{h_y}{u}; \quad u = \sin \theta - h_x \cos \theta, \quad (3.3-38)$$

where h_x and h_y are the surface slopes in the range (cross-track) and azimuth (along-track) directions, respectively. Note that these expressions are completely general; no assumptions are made about the form of the scattering matrix. In the special case where the range slopes are small, the rotation is directly proportional to the azimuth slope. Performing the transformation, we find that

$$\begin{aligned} \langle S_{hh}(\varphi) S_{hv}^*(\varphi) \rangle + \langle S_{hv}(\varphi) S_{vv}^*(\varphi) \rangle &= \frac{1}{2} \sin 2\varphi \left(\langle S_{hh} S_{hh}^* \rangle - \langle S_{vv} S_{vv}^* \rangle \right) \\ &+ \frac{1}{2} (1 + \cos 2\varphi) \left(\langle S_{hh} S_{hv}^* \rangle - \langle S_{hv} S_{vv}^* \rangle \right) \\ &- \frac{1}{2} (1 - \cos 2\varphi) \left(\langle S_{hv} S_{hh}^* \rangle - \langle S_{vv} S_{hv}^* \rangle \right) \end{aligned} \quad (3.3-39)$$

If the terrain exhibits reflection symmetry, the second and third terms are zero and this quantity becomes a real number. In that case, the estimate of the helix component as given by Eq. (3.3-29) will be zero. If the terrain does not exhibit reflection symmetry or if we only average over a relatively small number of pixels (recall that reflection symmetry only says that in the average the co-cross product will be zero) the estimate of the helix component will be

$$\begin{aligned} f_c &= 2 \left| \text{Im} \left\{ \langle S_{hh}(\varphi) S_{hv}^*(\varphi) \rangle + \langle S_{hv}(\varphi) S_{vv}^*(\varphi) \rangle \right\} \right| \\ &= \left| \text{Im} \left\{ (1 + \cos 2\varphi) \left(\langle S_{hh} S_{hv}^* \rangle - \langle S_{hv} S_{vv}^* \rangle \right) - (1 - \cos 2\varphi) \left(\langle S_{hv} S_{hh}^* \rangle - \langle S_{vv} S_{hv}^* \rangle \right) \right\} \right| \end{aligned} \quad (3.3-40)$$

This quantity is clearly modulated by the along-track slopes, so the results in the image on the right in Fig. 3-15 are not surprising.

3.3.2.3 The Non-Negative Eigenvalue Decomposition (NNED). The results in the previous two sections show a significant flaw in these decompositions; some negative powers might result after subtraction of the volume components from the observation. This is clearly a non-physical result. If the hypothesis is that the observed radar cross-section is the linear sum of radar cross-sections representing different types of scattering mechanisms, a crucial requirement is that each scattering mechanism must represent a physically realizable scatterer or collection of scatterers. This must also mean that the radar cross-section representing each scattering mechanism must be zero or positive for all polarization combinations. As shown in Eq. (3.1-5), this implies that all eigenvalues of the matrices representing the individual scattering processes must be non-negative. A decomposition method that takes this property into account was proposed by van Zyl et al. (2008) [13] and van Zyl et al. (2010) [14], which we shall call the non-negative eigenvalue decomposition (NNED).

To introduce the NNED technique, let us take a more generic decomposition where we want to express the scattering as follows

$$\langle [\mathbf{C}] \rangle = a[\mathbf{C}_{model}] + [\mathbf{C}_{remainder}]. \quad (3.3-41)$$

Here, the first term on the right represents the covariance matrix predicted by some model, such as randomly oriented branches. Recognizing that the form of this covariance matrix might be different from the measured matrix, we add the second term, which will contain whatever is in the measured matrix that is not consistent with the model matrix. The question now is what value of a to use in Eq. (3.3-41). To answer this question, we need to recognize that all matrices in Eq. (3.3-41) must represent physically realizable covariance matrices. That is, if we look at each matrix by itself, it should satisfy all the restrictions that we expect for a measured covariance matrix. In particular, we need to insist that the eigenvalues for each matrix are real and greater than or equal to zero. Let us rewrite Eq. (3.3-41) in the form

$$[\mathbf{C}_{remainder}] = \langle [\mathbf{C}] \rangle - a[\mathbf{C}_{model}]. \quad (3.3-42)$$

The matrix on the left must have eigenvalues that are real and are larger than or equal to zero. This requirement allows us to derive a limit on the values of a . The largest value of a that still ensures that all three eigenvalues of the matrix on the left would be greater than or equal to zero is the maximum value of a that we could use in Eq. (3.3-41).

To derive the general expressions limiting the values of a , we start with the average covariance matrix for terrain with reflection symmetry as given in Eq. (3.3-11) and write the model covariance matrix as

$$[\mathbf{C}_{model}] = \begin{pmatrix} \xi_a & 0 & \rho_a \\ 0 & \eta_a & 0 \\ \rho_a^* & 0 & \zeta_a \end{pmatrix}. \quad (3.3-43)$$

Then Eq. (3.3-42) becomes

$$[\mathbf{C}_{remainder}] = \begin{pmatrix} \xi & 0 & \rho \\ 0 & \eta & 0 \\ \rho^* & 0 & \zeta \end{pmatrix} - a \begin{pmatrix} \xi_a & 0 & \rho_a \\ 0 & \eta_a & 0 \\ \rho_a^* & 0 & \zeta_a \end{pmatrix}. \quad (3.3-44)$$

The eigenvalues for this matrix are the roots of the following equation

$$(\eta - a\eta_a - \lambda) \left\{ \lambda^2 - (\xi + \zeta - a\xi_a - a\zeta_a)\lambda + (\xi - a\xi_a)(\zeta - a\zeta_a) - |\rho - a\rho_a|^2 \right\} = 0, \quad (3.3-45)$$

which are

$$\begin{aligned} \lambda_1 &= \frac{1}{2} \left\{ \xi + \zeta - a\xi_a - a\zeta_a + \sqrt{(\xi + \zeta - a\xi_a - a\zeta_a)^2 - 4(\xi - a\xi_a)(\zeta - a\zeta_a) + 4|\rho - a\rho_a|^2} \right\} \\ \lambda_2 &= \frac{1}{2} \left\{ \xi + \zeta - a\xi_a - a\zeta_a - \sqrt{(\xi + \zeta - a\xi_a - a\zeta_a)^2 - 4(\xi - a\xi_a)(\zeta - a\zeta_a) + 4|\rho - a\rho_a|^2} \right\}. \\ \lambda_3 &= \eta - a\eta_a \end{aligned} \quad (3.3-46)$$

Since $\lambda_1 \geq \lambda_2$, the maximum value of a is found when either $\lambda_2 = 0$ or when $\lambda_3 = 0$. To find the value of a that would make $\lambda_2 = 0$, we need to solve the equation

$$\begin{aligned} (\xi - a\xi_a)(\zeta - a\zeta_a) &= |\rho - a\rho_a|^2 \\ \Rightarrow (\xi_a\zeta_a - |\rho_a|^2)a^2 - \{(\xi\zeta_a + \zeta\xi_a) - \rho\rho_a^* - \rho^*\rho_a\}a + \xi\zeta - |\rho|^2 &= 0 \end{aligned} \quad (3.3-47)$$

This quadratic has two roots that are both positive. The smaller of the two is

$$a = \frac{1}{2(\xi_a\zeta_a - |\rho_a|^2)} \left\{ (\xi\zeta_a + \zeta\xi_a) - \rho\rho_a^* - \rho^*\rho_a - \sqrt{[(\xi\zeta_a + \zeta\xi_a) - \rho\rho_a^* - \rho^*\rho_a]^2 - 4(\xi_a\zeta_a - |\rho_a|^2)(\xi\zeta - |\rho|^2)} \right\}. \quad (3.3-48)$$

The case of $\lambda_3 = 0$ is straightforward. The resulting maximum a is, therefore,

$$a_{\max} = \min \left\{ \frac{\eta/\eta_a}{2(\xi_a \zeta_a - |\rho_a|^2)} \left\{ (\xi \zeta_a + \zeta \xi_a) - \rho \rho_a^* - \rho^* \rho_a \right. \right. \quad (3.3-49)$$

$$\left. \left. - \sqrt{\left[(\xi \zeta_a + \zeta \xi_a) - \rho \rho_a^* - \rho^* \rho_a \right]^2 - 4(\xi_a \zeta_a - |\rho_a|^2)(\xi \zeta - |\rho|^2)} \right\} \right\}$$

It should be pointed out that in the general form for the model matrix we assumed in Eq. (3.3-43), we have explicitly assumed that the model matrix represents an average scattering process for terrain with reflection symmetry. It also includes cases of a single scatterer with no cross-polarized component, such as a pure dihedral or first-order scattering from a slightly rough surface. It does not, however, include scattering from terrain that does not exhibit reflection symmetry or single scatterers with cross-polarized components. For those cases, the expressions become significantly more complicated, with the eigenvalues being the roots to a cubic polynomial. However, most observed scattering seems to approximate reflections symmetry well, as evidenced by the relatively small values of the helix component in the Yamaguchi et al. (2005) [10] decomposition discussed in the previous section; therefore, we do not believe the current analysis to be too severely limited by these assumptions. In any case, the fundamental approach remains the same. We always insist that no eigenvalue be negative.

We note that if the model represents a single scatterer with no cross-polarized return, $\xi_a \zeta_a = |\rho_a|^2$ and we can simplify the expressions in Eq. (3.3-49) to

$$a_{\max} = \min \left\{ \frac{\eta/\eta_a}{\frac{\xi \zeta - |\rho|^2}{(\xi \zeta_a + \zeta \xi_a) - \rho \rho_a^* - \rho^* \rho_a}} \right\}. \quad (3.3-50)$$

Let's illustrate this process with an example. For the model, we shall assume a uniformly random oriented cloud of thin cylinders. The expression for the average covariance matrix for this model was derived in Chapter 2 and for the backscatter case is given by

$$\langle [\mathbf{C}_{cylinders}] \rangle = \begin{pmatrix} 3/8 & 0 & 1/8 \\ 0 & 2/8 & 0 \\ 1/8 & 0 & 3/8 \end{pmatrix}. \quad (3.3-51)$$

Putting these together in Eq. (3.3-49), we find the resulting maximum a is, therefore,

$$a_{\max} = \min \left\{ \frac{4\eta}{2} \left\{ 3(\xi + \zeta) - \rho - \rho^* - \sqrt{[3(\xi + \zeta) - \rho - \rho^*]^2 - 32(\xi\zeta - |\rho|^2)} \right\} \right\}. \quad (3.3-52)$$

To illustrate this process with a numerical example, consider the case of a covariance matrix extracted from the Black Forest image at L-band. The normalized matrix is

$$\langle [\mathbf{C}] \rangle = \begin{pmatrix} 0.472 & 0.008 + i0.010 & 0.056 - i0.029 \\ 0.008 - i0.010 & 0.235 & 0.003 - i0.002 \\ 0.056 + i0.029 & 0.003 + i0.002 & 0.293 \end{pmatrix}. \quad (3.3-53)$$

Note that this matrix is not the same as the one we assumed in Eq. (3.3-11), but the terms assumed to be zero in Eq. (3.3-11) are indeed much smaller than the others. We shall, therefore, ignore those terms and effectively set them equal to zero, consistent with what Freeman and Durden (1998) [9] assumed. Using Eq. (3.3-52), we find that

$$a_{\max} = \min(0.940, 0.752) = 0.752. \quad (3.3-54)$$

Simply setting the strength of the returns from the randomly oriented cylinders based on the cross-polarized return will force us to use the value 0.940 for a . Clearly, this is much larger than the allowable value of 0.752. Using this maximum value of a , we find that the decomposition would be

$$\begin{pmatrix} 0.472 & 0.008 + i0.010 & 0.056 - i0.029 \\ 0.008 - i0.010 & 0.235 & 0.003 - i0.002 \\ 0.056 + i0.029 & 0.003 + i0.002 & 0.293 \end{pmatrix} \approx \begin{pmatrix} 0.281 & 0 & 0.094 \\ 0 & 0.188 & 0 \\ 0.094 & 0 & 0.281 \end{pmatrix} + \begin{pmatrix} 0.191 & 0 & -0.038 - i0.029 \\ 0 & 0.047 & 0 \\ -0.038 + i0.029 & 0 & 0.012 \end{pmatrix}. \quad (3.3-55)$$

Figure 3-16 shows a comparison of the fraction of the scattering assigned to the randomly oriented canopy by using the approach suggested by Freeman and Durden (1998) [9] and that using the maximum value of a as we have described above. The fraction is expressed as the total power of the scattering from the randomly oriented cloud of cylinders as compared to the total power in the measured covariance matrix. In the case of the Freeman and Durden (1998) [9] decomposition, this ratio is simply the thin vegetation index, as defined in Eq. (3.2-3). We note from this figure that the fraction of scattering that should be assigned to the vegetation is generally quite a bit lower than if we simply assume that all the cross-polarized scattering comes from the randomly oriented branches. In fact, on the average, the maximum amount of scattering from the

branches is between 10 and 20 percent lower if we insist that the eigenvalues remain positive. Nevertheless, the random scattering clearly still dominates in the vegetated areas; this correction would not change the qualitative interpretation of the scattering for this scene significantly.

It is important to remember that the image on the right in Fig. 3-16 represents the maximum amount of scattering we can assign to the randomly oriented cylinders. We are, of course, free to assign less than that, and we would not violate our requirement that the eigenvalues of the remainder not be negative. This result points to one of the difficulties with model-based decompositions: How are we to decide how much of the scattering to assign to the randomly oriented cylinders? Unfortunately, there is no simple answer to this question. A reasonable suggestion is to use the amount of power in the left-over matrix (that is, the one labeled “remainder” in Eq. (3.3-41)) as a guide. One could make the argument that the best value of a to use would be that value of a that results in the minimum amount of power in the remainder matrix. We can then simply compare the total power in the remainder matrix to that in the original measurement and select that value of a that minimizes this ratio. For the single-

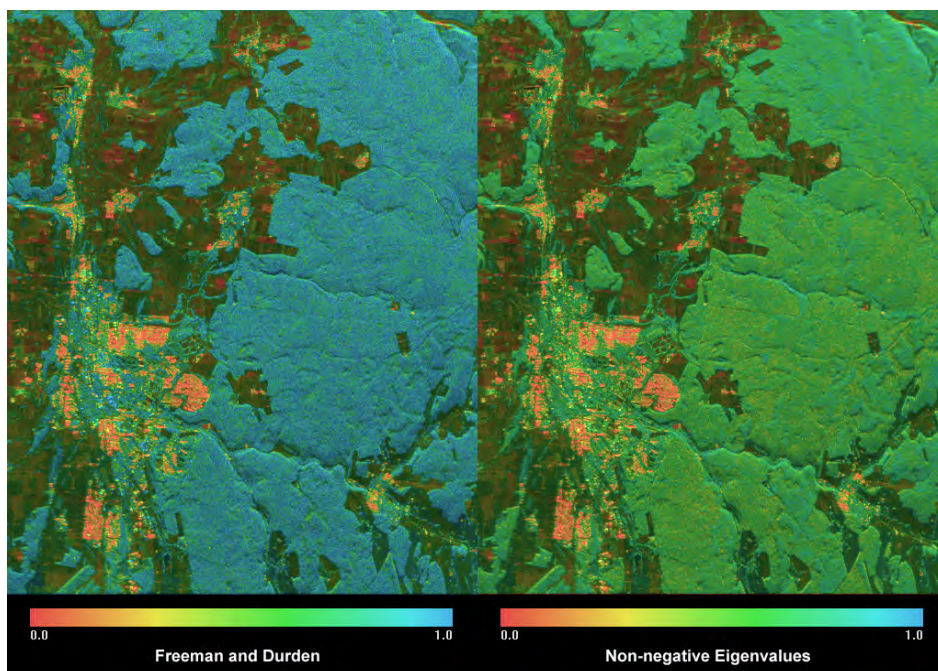


Fig. 3-16. These images display the fraction of the observed total power that can be attributed to scattering from a uniformly randomly oriented layer of cylinders. The image on the left follows the calculation proposed by Freeman and Durden (1998) [9]. The image on the right is calculated by requiring that the remaining eigenvalues not be negative. On the average, the image on the right shows about 10-20 percent lower values for the forested areas than the one on the left.

model case discussed so far, this simply leads to picking the maximum value of a .

The question now is whether there is a way to pick the “best” solution for a generic model-based decomposition for vegetation scattering. We shall assume, like Freeman and Durden (1998) [9], that the scattering from vegetated terrain consists of three major components: scattering from the canopy, double reflection scattering, and single reflections from the underlying ground surface. We then propose a hybrid approach that combines model-based decomposition and eigenvalue decomposition. In the case of the Freeman and Durden (1998) [9] decomposition, they must artificially decide whether to explicitly solve for the double-reflection or the single-reflection parameters by examining the phase difference between HH and VV. As we showed before (van Zyl, 1992 [15]), the eigenvalue decomposition itself can be interpreted in terms of single (or odd numbers of) reflections, double (or even numbers of) reflections, and a diffuse part. Our hybrid approach then is as follows. We first subtract a covariance matrix representing a model for canopy scattering from the observed covariance matrix. We pick that multiplicative parameter that minimizes the power in the remainder matrix. We then perform an eigenvalue decomposition on the remainder matrix. Mathematically this translates to

$$\langle [C] \rangle = f_c [C_{canopy}] + \lambda_d [C_{double}] + \lambda_s [C_{single}] + \lambda_r [C_{remainder}]. \quad (3.3-56)$$

Here, λ_r is the “diffuse” part of the covariance matrix that is left once we subtracted the canopy contribution to the observed scattering. It is clear that if we want to minimize the power in the last matrix on the right, we need to maximize the value of f_c . This is done using the expressions in Eq. (3.3-49), where the subscript a in that expression is substituted for the canopy model covariance matrix.

This decomposition needs only one assumption: that of the model to use to represent the canopy scattering. We no longer have to artificially make assumptions about the ratio of the HH to VV scattering strength for the double-reflection or single-reflection terms. These are determined by the eigenvectors of the matrix that is left over once the canopy contribution is subtracted.

Figure 3-17 shows a comparison of the Freeman and Durden (1998) [9] decomposition and NNED using uniformly randomly oriented thin cylinders as the model for the canopy scattering like Freeman and Durden. In our display of the NNED, we use the green color to show the canopy strength, blue to show the single scattering term, and red to show the double reflection term. We do not include the last term on the right in Eq. (3.3-56) in our display. At first look, these images are qualitatively very similar. A closer examination, however, shows that the details in the forested area are quite different. For example, there



Fig. 3-17. These L-band images show a comparison between a three-component decomposition as proposed by Freeman and Durden (left image) [9] and a modified version that ensures non-negative powers after the vegetation scattering has been subtracted (right image). Note the increased double reflections in the forested areas in the image on the right.

are significantly more double reflections in much of the forest in the modified three-component analysis (NNED) than in the original Freeman and Durden decomposition. This is to be expected, since we have now assigned less of the scattered power to the randomly oriented cylinders. Therefore, while the results are qualitatively the same, these images are quite different. This could be quite significant if one were to use these decomposed signals in further analysis to infer geophysical parameters.

Figure 3-18 shows a similar result calculated using the C-band images. The differences in the forest are now even more evident between the standard Freeman-Durden (1998) [9] decomposition and the modified version that ensures that all eigenvalues remain non-negative. In this case, there is significantly more scattering assigned to the single reflection model, especially in the older, higher biomass parts of the forest. This should not, however, be interpreted that there is more direct scattering observed from the ground surface under the forest. In fact, this increase is due to the fact that the thin cylinder model is less appropriate at C-band because most of the branches are no longer much thinner than the radar wavelength. When this happens, the random cylinder model matrix becomes more like scattering from a flat plate or a sphere. In the limiting case where the branches become much thicker than the

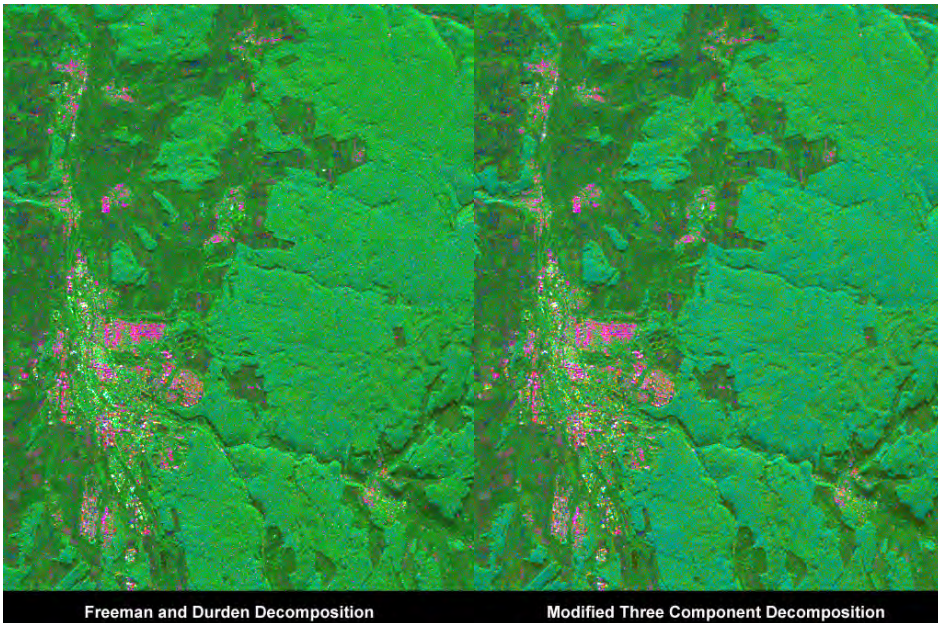


Fig. 3-18. Comparison between a three-component decomposition as proposed by Freeman and Durden (left image) and the modified version that ensures non-negative powers after the vegetation scattering has been subtracted (right image) at C-band. Note the increased single reflections in the forested areas in the image on the right. See the text for a discussion.

radar wavelength, the scattering from the randomly oriented thick branches would be indistinguishable from the scattering from a sphere or a flat plate.

Figure 3-19 shows the comparison at P-band. The modified decomposition shows significantly less random scattering and increased double reflections when compared to the Freeman-Durden (1998) [9] decomposition. This shows again how assigning all the cross-polarized return to the canopy scattering tends to overestimate the contribution from the canopy scattering. Also note that the scattering near the top of the image (the portion where the angle of incidence is quite steep) has a more bluish tint in the image on the right, implying more single scattering from the underlying ground surface. This is consistent with the expectation that at steeper angles of incidence the attenuation loss through the canopy will be lower, increasing the strength of the reflection from the underlying ground surface.

In all the discussion thus far we have implicitly assumed that the covariance matrix terms that involve cross-products of co-polarized returns and cross-polarized returns are negligibly small. The usual argument in favor of this assumption is that natural terrain tends to exhibit reflection symmetry over large scales. Yamaguchi et al. (2005) [10] point out that this is not always the

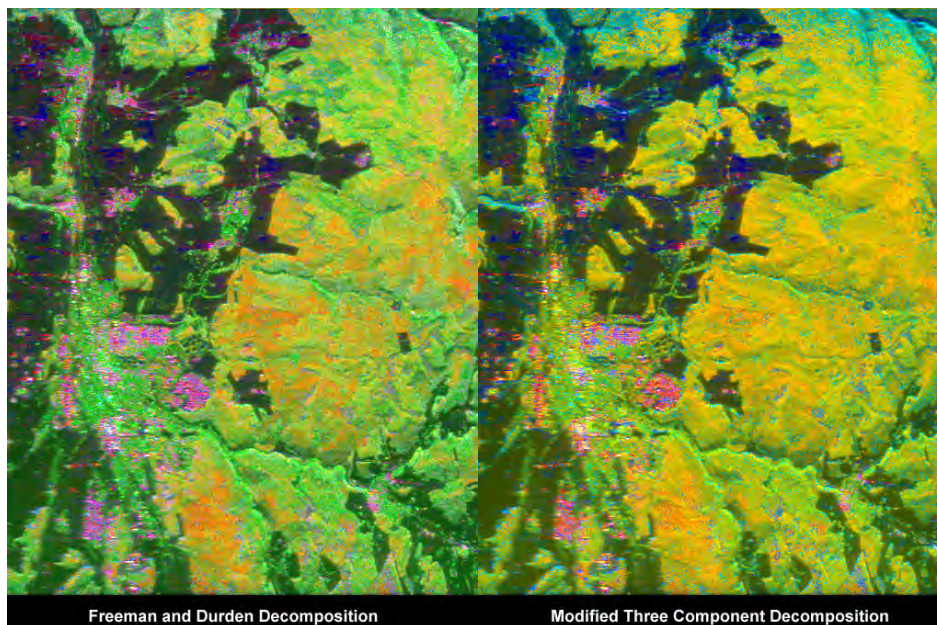


Fig. 3-19. Comparison between a three-component decomposition as proposed by Freeman and Durden (left image) and the modified version that ensures non-negative powers after the vegetation scattering has been subtracted (right image) at P-band. Note the increased double reflections (red color) in the forested areas in the image on the right.

case. In fact, they show examples of urban areas where these terms are not negligible. Their solution is to add a fourth model to the decomposition that includes scattering by helices to account for the observed correlation between the co-polarized and cross-polarized returns. They then proceed to first remove this helix component that is calculated based on the observed correlation. Note that our proposed hybrid decomposition as shown in Eq. (3.3-56) explicitly includes any potential observed cross-correlation between the co-polarized and cross-polarized components. The matrices that are calculated using the eigenvalue decomposition are formed from the eigenvectors of the covariance matrix that results from the subtraction of the assumed canopy model from the observed covariance matrix. Any correlation between the cross-polarized and co-polarized returns will result in these eigenvectors not being “pure” single, double, or diffuse scattering covariance matrices. The advantage of the NNED approach is that we do not have to assume a specific scattering mechanism that accounts for these observed correlations.

3.3.2.4 Adaptive Model-Based Decomposition. In the previous section, we laid out a method for performing a model-based decomposition that ensures that all the individual matrices have non-negative eigenvalues. We shall now show

how this same idea can be used to determine which canopy model is the “best” fit to the observations.

As we pointed out before, the idea is to minimize the amount of power in the matrix that is left once we subtract the canopy scattering. This provides a simple way to compare different canopy models. We simply calculate the amount of power that would be in the remainder matrix once we subtract each canopy model contribution. The model with the smallest amount of power left over is then assumed to be the best fit to the observation. In fact, Yamaguchi et al. (2005) [10] pointed out that the uniformly randomly oriented cloud of thin cylinders might not always be the appropriate model for canopy scattering. As part of their four-component scattering decomposition, they included a test to apply different canopy models.

As an illustration of the idea, let us first look at an example where we will use a limited number of different canopy models to find the best fit for the L-band data of the Black Forest image we have been analyzing so far. In doing the test, we assume three different models: a uniformly randomly oriented cloud of thin cylinders, a cloud of thin cylinders oriented around the horizontal direction with a cosine squared distribution, and a cloud of thin cylinders oriented around the vertical direction with a cosine squared distribution. For each pixel in the image, we then calculate the relative amount of power in the remainder matrix if we subtracted the maximum contribution assuming each of these models. Figure 3-20 shows the result for the three cases at L-band. At the global scale of the image, it appears that the best fit model at L-band might be the cosine

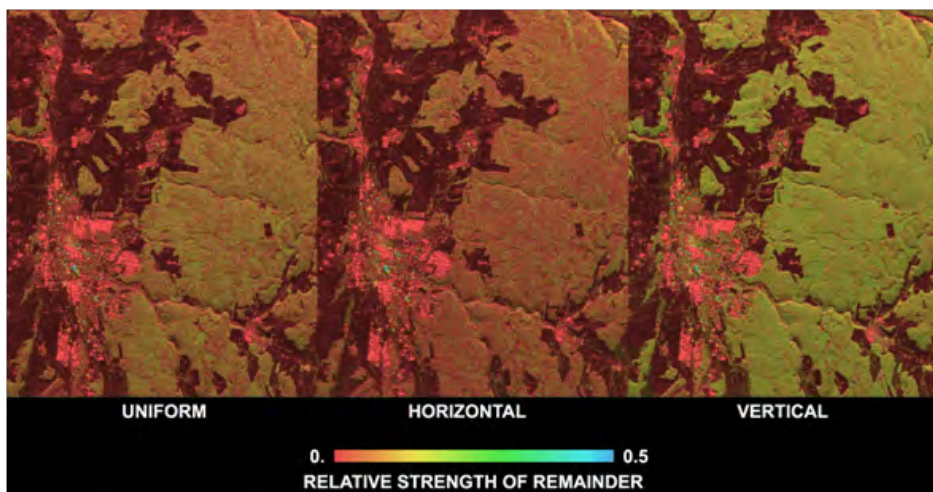


Fig. 3-20. Comparison of different canopy models at L-band. The images show the relative amount of power in the remainder matrix after the canopy contribution has been subtracted from the observation. The results show that the cosine squared distribution around the horizontal orientation provides the best fit over the majority of the image.

squared distribution around the horizontal orientation. Most of the image is, in fact, coniferous trees with branches that are closer to horizontal orientation than uniformly randomly oriented; this result is, therefore, not unexpected.

It should be pointed out that this result cannot be taken as conclusive proof that the canopy contains branches that have orientations that are closer to horizontal. In drawing such conclusions, one has to remember that this result shows the best fit of a canopy model to the observation by first subtracting the canopy contribution. In some sense, this means we assume that the scattering is dominated by the canopy contribution. If, for example, we had the case of a pure double reflection (for which HH is larger than VV) with a small contribution from a uniformly oriented canopy, the resulting covariance matrix would have HH larger than VV. In that case, we might find that the best fit canopy model is a cosine squared around the horizontal orientation because that model predicts that HH will be larger than VV.

We can now extend this concept by adaptively performing the decomposition on each pixel to find the best canopy model for that pixel. The process is the same as we described above, except it is performed for each pixel separately. For each pixel, we now compare the remainders for the set of models and pick the model that leaves the smallest relative amount of power in the remainder after we subtract the canopy contribution. We shall first introduce this concept with just the three models described above (the same three used by Yamaguchi et al. (2005) [10]) and later generalize the concept. Figure 3-21 shows the results for the Black Forest image at C-band, L-band, and P-band. At C-band,

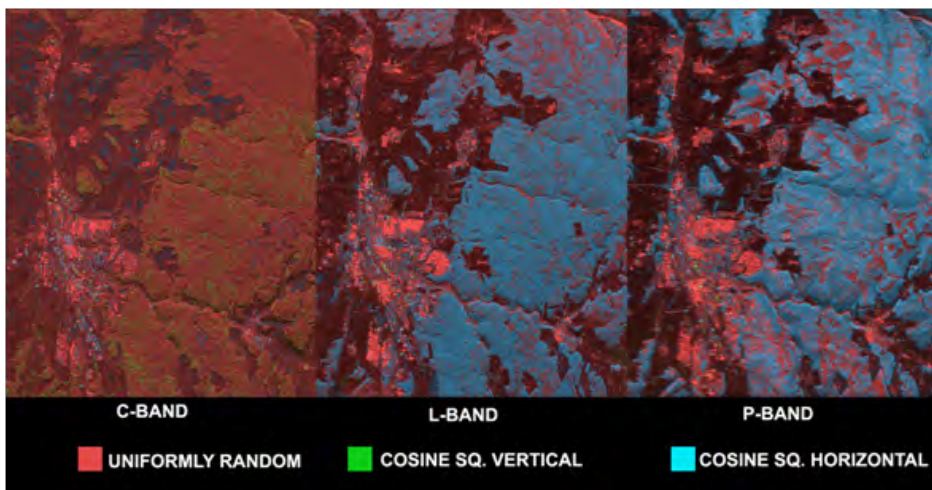


Fig. 3-21. Adaptive non-negative eigenvalue decompositions at different frequencies with three canopy scattering models. At the longer wavelengths, the scattering is best modeled by a cosine squared distribution around the horizontal orientation. At C-band, a uniformly random orientation provides the best fit. See the text for more discussion.

the uniformly randomly oriented model is the best fit, consistent with scattering from the needles in the coniferous trees. At L-band and P-band, we see that most of the pixels are better represented by a model with a cosine-squared distribution around the horizontal orientation. At L-band this result is likely because of the primary branch orientation. At P-band, however, this is probably more indicative that double-bounce scattering from the ground surface and tree trunks likely dominates.

Figure 3-22 shows the L-band comparison of the adaptive decomposition using three models compared to the Yamaguchi et al. (2005) [10] choice of model based on their simplified selection criteria involving the ratio of HH to VV power. We have blanked out pixels for which either the single reflections or the double reflections are stronger than the canopy component since, for those pixels, our original assumption that the canopy scattering dominates clearly does not hold. First, we notice a difference in the number of pixels that are blanked out between the adaptive decomposition and the Yamaguchi et al. decomposition. This is primarily related to the amount of power assigned to the canopy component and the fact that for our adaptive decomposition we insist that all eigenvalues be non-negative. This will typically assign less power to the canopy component. Apart from this difference, however, it is obvious that the two adaptive techniques give very similar results.

Building on these initial results, Ariei et al. (2010) [16] and Ariei (2009) [17] extended the adaptive decomposition technique to include a generalized canopy

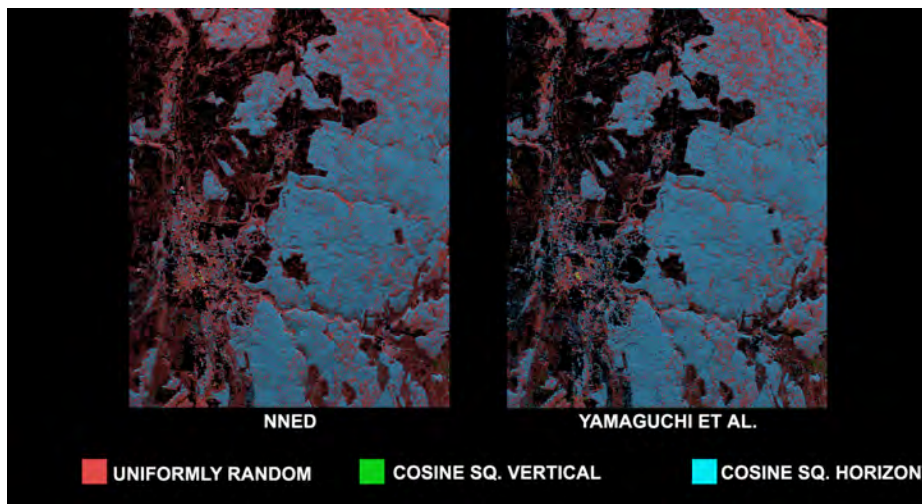


Fig. 3-22. This figure shows a comparison of the optimum model indicated by the color schemes for the adaptive NNED and Yamaguchi et al. models using the L-band image. We have blanked out those pixels for which the canopy scattering is not the strongest component. Note the great similarity between the NNED and Yamaguchi results in terms of which models best represents the canopy scattering.

component that selects the best fit to the canopy scattering over different amounts of randomness and different mean orientations of the canopy. Their characterization of the canopy scattering starts with the scattering matrix of a vertically oriented thin cylinder, which apart from a multiplicative constant that depends on the cylinder length and dielectric constant, can be written as

$$[S_{cyl}] \propto \begin{bmatrix} 0 & 0 \\ 0 & 1 \end{bmatrix}. \quad (3.3-57)$$

They then allow this cylinder to be rotated by an angle θ with respect to the vertical direction about the line of sight, with positive values of θ indicating a clockwise rotation. The resulting covariance matrix is found to be

$$[C_{cyl}(\theta)] = \frac{1}{4} \begin{pmatrix} (1 - \cos 2\theta)^2 & \sqrt{2} \sin 2\theta(1 - \cos 2\theta) & \sin^2 2\theta \\ \sqrt{2} \sin 2\theta(1 - \cos 2\theta) & 2 \sin^2 2\theta & \sqrt{2} \sin 2\theta(1 + \cos 2\theta) \\ \sin^2 2\theta & \sqrt{2} \sin 2\theta(1 + \cos 2\theta) & (1 + \cos 2\theta)^2 \end{pmatrix}. \quad (3.3-58)$$

They write this as the sum of three matrices:

$$[C_{cyl}(\theta)] = \frac{1}{8} \begin{pmatrix} 3 & 0 & 1 \\ 0 & 2 & 0 \\ 1 & 0 & 3 \end{pmatrix} + \frac{2}{8} \begin{pmatrix} -2 \cos 2\theta & \sqrt{2} \sin 2\theta & 0 \\ \sqrt{2} \sin 2\theta & 0 & \sqrt{2} \sin 2\theta(1 + \cos 2\theta) \\ 0 & \sqrt{2} \sin 2\theta & 2 \cos 2\theta \end{pmatrix} \\ + \frac{1}{8} \begin{pmatrix} \cos 4\theta & -\sqrt{2} \sin 4\theta & -\cos 4\theta \\ -\sqrt{2} \sin 4\theta & -2 \cos 4\theta & \sqrt{2} \sin 4\theta \\ -\cos 4\theta & \sqrt{2} \sin 4\theta & \cos 4\theta \end{pmatrix}. \quad (3.3-59) \\ = [C_\alpha] + 2[C_\beta(2\theta)] + [C_\gamma(4\theta)]$$

The next step is then to calculate the average covariance matrix for a given probability distribution of the cylinder orientation angles. The resulting average covariance matrix is

$$\langle [C_{vol}] \rangle = \int_0^{2\pi} [C_{cyl}(\theta)] p(\theta) d\theta, \quad (3.3-60)$$

where $p(\theta)$ describes the probability density function of the cylinder orientation angles. In the discussion above, we have used three cases: uniform distribution for which

$$p_{uniform} = \frac{1}{2\pi} \quad (3.3-61)$$

and cosine-squared distributions around the vertical and horizontal directions are as follows

$$p_{\cos_sq} = \frac{\cos^2(\theta - \theta_0)}{2\pi \int_0^{2\pi} \cos^2(\theta - \theta_0) d\theta}. \quad (3.3-62)$$

For the distribution peaking around vertical, $\theta_0 = 0$; while for the horizontal case, $\theta_0 = \pi/2$. The uniform distribution represents the most random orientation. In the other extreme, the delta function around a fixed angle

$$p_{delta} = \frac{1}{2} \{ \delta(\theta - \theta_0) + \delta(\theta - \theta_0 - \pi) \} \quad (3.3-63)$$

represents the least amount of randomness. Arii (2009) [17] and Arii et al. (2010) [18] suggested that all these cases can be approximated by a generalized n -th power cosine squared distribution, as follows:

$$p_v(\theta, \theta_0, n) = \frac{\{ \cos^2(\theta - \theta_0) \}^n}{2\pi \int_0^{2\pi} \{ \cos^2(\theta - \theta_0) \}^n d\theta}. \quad (3.3-64)$$

When $n = 0$, this distribution becomes exactly the same as the uniform distribution; specifically, it approximates the delta function distribution with infinitely large n .

The average covariance matrix for the generalized probability density function can be written as

$$\langle [C_{vol}(\theta_0, n)] \rangle = \frac{1}{A_n} \int_0^{2\pi} [C_{cyl}(\theta)] \cos^{2n}(\theta - \theta_0) d\theta, \quad (3.3-65)$$

with

$$A_n = \int_0^{2\pi} \cos^{2n}(\theta - \theta_0) d\theta. \quad (3.3-66)$$

To derive expressions for these, we note that we can write

$$\cos^{2n} x = \frac{1}{2^{2n}} \binom{2n}{n} + \frac{1}{2^{2n-1}} \sum_{k=0}^{n-1} \binom{2n}{k} \cos 2(n-k)x. \quad (3.3-67)$$

Using the series expansion in Eq. (3.3-67), we find

$$A_n = \frac{\pi}{2^{2n-1}} \binom{2n}{n}. \quad (3.3-68)$$

Also, note that

$$\begin{aligned} \int_0^{2\pi} [C_{cyl}(\theta)] \cos^{2n}(\theta - \theta_0) d\theta &= \frac{1}{2^{2n}} \binom{2n}{n} \int_0^{2\pi} [C_{cyl}(\theta)] d\theta \\ &+ \frac{1}{2^{2n-1}} \sum_{k=0}^{n-1} \binom{2n}{k} \int_0^{2\pi} [C_{cyl}(\theta)] \cos\{2(n-k)(\theta - \theta_0)\} d\theta \end{aligned} \quad (3.3-69)$$

It is easily shown that

$$\frac{1}{2^{2n}} \binom{2n}{n} \int_0^{2\pi} [C_{cyl}(\theta)] d\theta = \frac{\pi}{2^{2n-1}} \binom{2n}{n} [C_\alpha]. \quad (3.3-70)$$

Next, we note that

$$\begin{aligned} \int_0^{2\pi} [C_{cyl}(\theta)] \cos\{2(n-k)(\theta - \theta_0)\} d\theta \\ = \cos\{2(n-k)\theta_0\} \int_0^{2\pi} [C_{cyl}(\theta)] \cos\{2(n-k)\theta\} d\theta \\ + \sin\{2(n-k)\theta_0\} \int_0^{2\pi} [C_{cyl}(\theta)] \sin\{2(n-k)\theta\} d\theta \end{aligned} \quad (3.3-71)$$

We easily find that

$$\int_0^{2\pi} [C_\alpha] \cos\{2(n-k)\theta\} d\theta = \int_0^{2\pi} [C_\alpha] \sin\{2(n-k)\theta\} d\theta = 0. \quad (3.3-72)$$

After considerable algebra, we find

$$\int_0^{2\pi} [C_\beta(2\theta)] \cos\{2(n-k)(\theta-\theta_0)\} d\theta = \begin{cases} 2\pi [C_\beta(2\theta_0)] & \text{for } k=n-1 \\ 0 & \text{otherwise} \end{cases} \quad (3.3-73)$$

$$\int_0^{2\pi} [C_\gamma(4\theta)] \cos\{2(n-k)(\theta-\theta_0)\} d\theta = \begin{cases} \pi [C_\gamma(4\theta_0)] & \text{for } k=n-2 \\ 0 & \text{otherwise} \end{cases}$$

Using Eq. (3.3-73), Eq. (3.3-72), Eq. (3.3-70), and Eq. (3.3-68) in Eq. (3.3-65), we find

$$\langle [C_{vol}(\theta_0, n)] \rangle = [C_\alpha] + \frac{2n}{n+1} [C_\beta(2\theta_0)] + \frac{n(n-1)}{(n+1)(n+2)} [C_\gamma(4\theta_0)]. \quad (3.3-74)$$

Note that we have derived this expression assuming that n is an integer. We have also verified this expression numerically for values of n that are not integers (Arii et al., 2010 [18]). For the three cases we have used so far, we find

$$\begin{aligned} \langle [C_{vol}^{uniform}] \rangle &= [C_\alpha] \\ \langle [C_{vol}^{cos_sq}(\theta_0)] \rangle &= [C_\alpha] + [C_\beta] \\ \langle [C_{vol}^{delta}(\theta_0)] \rangle &= [C_\alpha] + 2[C_\beta] + [C_\gamma] \end{aligned} \quad (3.3-75)$$

The eigenvalues of the covariance matrix in Eq. (3.3-74) only depend on the value of the power of the cosine squared function and not on the mean orientation angle. The eigenvalues are:

$$\begin{aligned} \lambda_1 &= \frac{1}{4(n+1)(n+2)} \left\{ 2n^2 + 4n + 3 + \sqrt{4n^2(n+2)^2 + (2n+1)^2} \right\} \\ \lambda_2 &= \frac{1}{4(n+1)(n+2)} \left\{ 2n^2 + 4n + 3 - \sqrt{4n^2(n+2)^2 + (2n+1)^2} \right\} \\ \lambda_3 &= \frac{1}{2} \frac{2n+1}{(n+1)(n+2)} \end{aligned} \quad (3.3-76)$$

Figure 3-23 shows the three eigenvalues as a function of the power of the cosine-squared function. Note that for all values of n , $\lambda_2 \leq \lambda_3 \leq \lambda_1$. This figure shows that there is little practical difference for distributions for values of $n > 20$. To illustrate this, we show the entropy and the RVI of the resulting average covariance matrix as a function of n in Fig. 3-24. The results confirm that especially the RVI varies very little for values of $n > 20$.

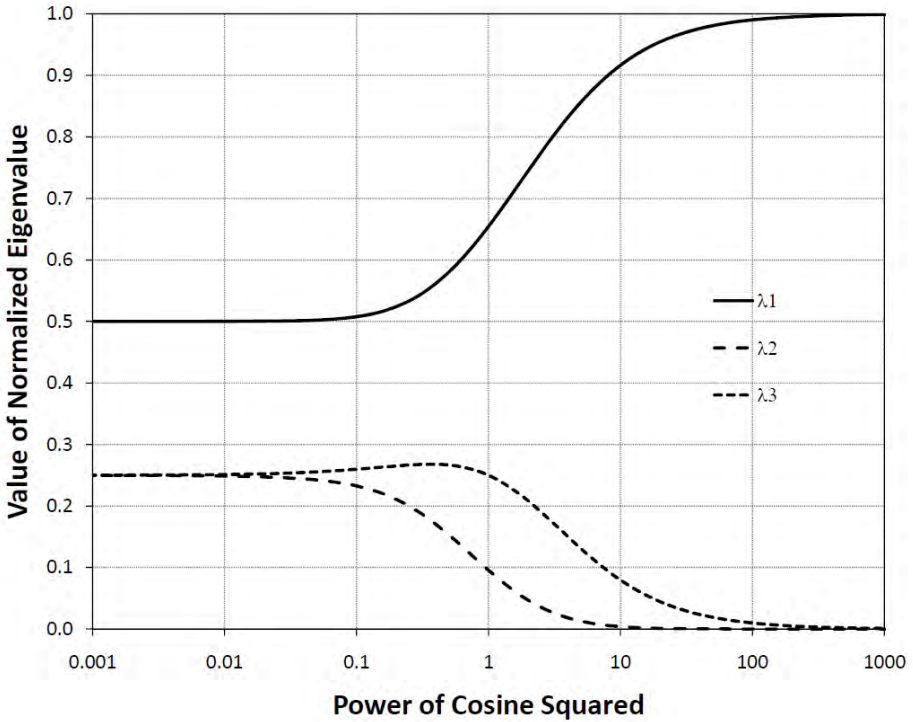


Fig. 3-23. This figure shows the relative strength of the eigenvalues of the covariance matrix representing the generalized volume scattering model. For all values of n , we find that $\lambda_2 \leq \lambda_3 \leq \lambda_1$.

With this theoretical framework in hand, we can now describe the proposed adaptive model-based decomposition. In fact, it differs from the previously described NNED only in the first step of the decomposition. Instead of choosing a specific model for the canopy scattering, the adaptive decomposition calculates the best fit over all powers n and all mean orientation angles θ_0 . We decide which pair of parameters represent the best fit by selecting that pair that results in the least amount of power in the “remainder” matrix:

$$\langle [C'_{remainder}] \rangle = \langle [C] \rangle - f_v \left\{ [C_\alpha] + \frac{2n}{n+1} [C_\beta] + \frac{n(n-1)}{(n+1)(n+2)} [C_\gamma] \right\}. \quad (3.3-77)$$

Note that the canopy distribution function as used here does not assume reflection symmetry. In fact, reflection symmetry only results for special mean orientation angles. As such, Eq. (3.3-77) describes a general decomposition; we do not need to resort to adding special scatterers to generate non-zero correlations between the cross- and co-polarized terms in the covariance matrix.

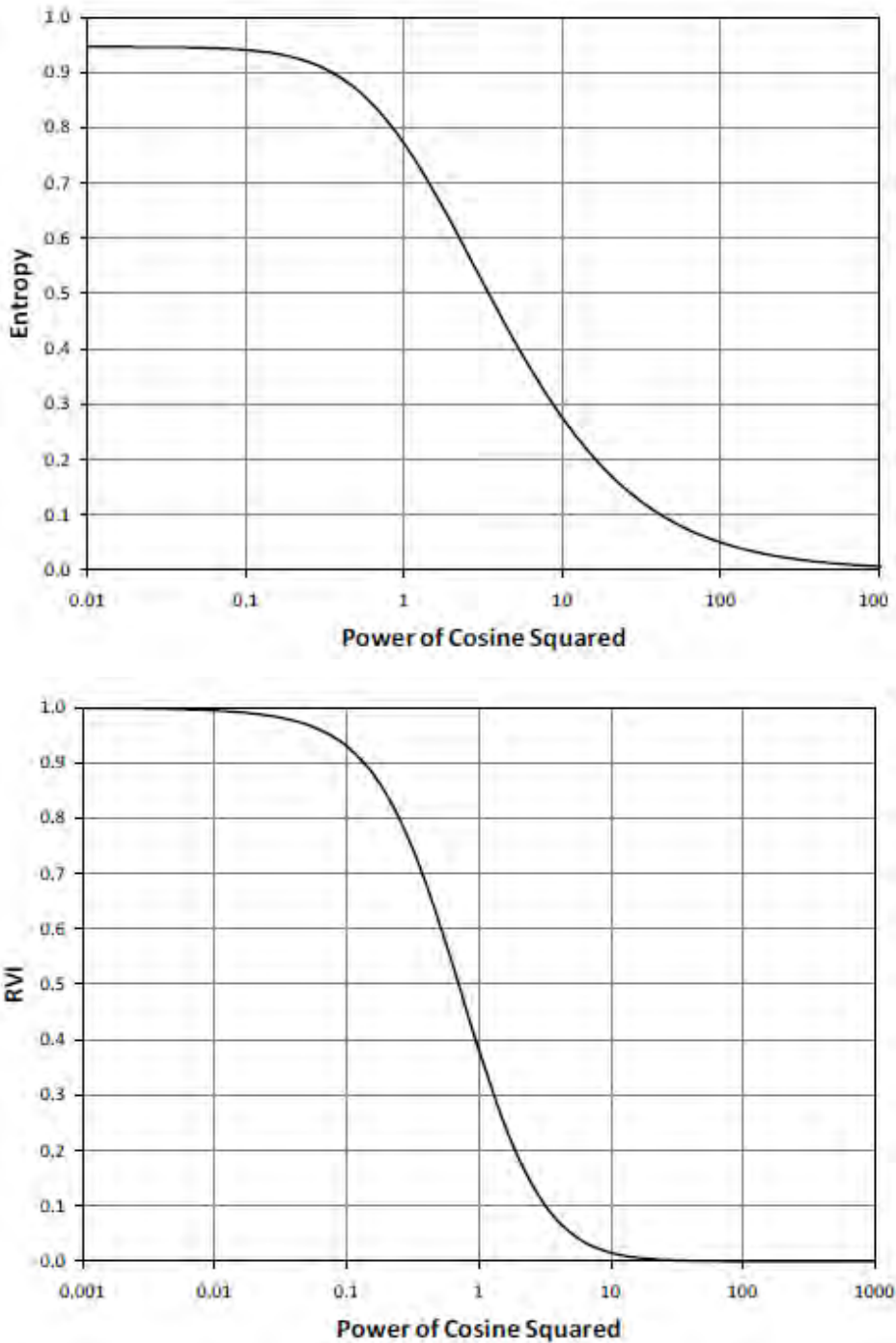


Fig. 3-24. Two charts showing the relative strength of the eigenvalues of the covariance matrix representing the generalized volume-scattering model. The top chart is a plot of entropy, and the bottom is a plot of RVI.

We first illustrate our results with a numerical example. For our comparison, we extracted the average covariance matrix in the forest portion of the Black Forest image at all three frequencies. The resulting matrices are

$$\begin{aligned} \langle C \rangle_C &= \begin{pmatrix} 0.36 & -0.07 + i0.0 & -0.18 - i0.03 \\ -0.07 - i0.0 & 0.20 & -0.08 + i0.0 \\ -0.18 + i0.03 & -0.08 - i0.0 & 0.44 \end{pmatrix} \\ \langle C \rangle_L &= \begin{pmatrix} 0.52 & -0.09 - i0.03 & -0.09 + i0.08 \\ -0.09 + i0.03 & 0.22 & -0.06 + i0.01 \\ -0.09 - i0.08 & -0.06 - i0.01 & 0.26 \end{pmatrix}. \\ \langle C \rangle_P &= \begin{pmatrix} 0.67 & -0.07 + i0.0 & -0.03 + i0.13 \\ -0.07 - i0.0 & 0.13 & -0.04 + i0.01 \\ -0.03 - i0.13 & -0.04 - i0.01 & 0.20 \end{pmatrix} \end{aligned} \quad (3.3-78)$$

We shall illustrate the use of this model by assuming the canopy scattering dominates and that we can consider the canopy as a collection of randomly oriented dipoles. This is equivalent to assuming that the scattering is from a collection of randomly oriented cylinders, but that the cylinders are much thinner than the radar wavelength.

In fitting our observations to the model, we use the methodology described above. The results are:

$$\begin{aligned} C - Band: \quad n &= 0.92 \quad \theta_0 = 143.4^\circ \\ L - Band: \quad n &= 1.66 \quad \theta_0 = 107.7^\circ. \\ P - Band: \quad n &= 3.47 \quad \theta_0 = 99.1^\circ \end{aligned} \quad (3.3-79)$$

These results show a decrease in randomness with an increase in wavelength. Also, the longer wavelengths sense a mean orientation angle that is close to horizontal (recall the angles are measured with respect to the orientation angle of a vertically oriented dipole). Since the longer wavelengths interact preferentially with the larger branches, which for the type of trees present in this data set are oriented closer to the horizontal direction, the results appear reasonable. The C-band results indicate more randomness, consistent with interactions with more vertically oriented needles that are also more randomly oriented than the larger branches.

Next we show the results of applying the adaptive decomposition to the Black Forest image. First we show the randomness results in Fig. 3-25. A significant difference is observed in the forested area as a function of wavelength,

consistent with the numerical example as reported in van Zyl et al. (2010) [14]. Randomness values close to that of the uniform distribution are found over the C-band image; conversely, the P-band image shows values with less randomness than cosine-squared distribution. From a physical point of view, this is reasonable considering the orientation distributions of needles, branches, and trunks. The shorter wavelength mainly interacts with the needles, which have higher variance than trunks and branches. Also, the P-band can penetrate needles and branches so that trunks having much lower variance become dominant. Some of the areas of increased randomness visible at P-band have previously been shown to be areas where the trunk scattering is reduced due to topographic effects (van Zyl, 1993 [5]). The L-band result lies in between these two cases; this corresponds mainly to the branch distribution.

Next, we show the mean orientation angle for all three frequencies in Fig. 3-26. Pixels with horizontal orientation are widely distributed in the forested area of the L- and P-band images. Before continuing with the interpretation, it is necessary to look at the decomposition results of all three scattering mechanisms, as in Fig. 3-27. Here, we display each scattering mechanism separately, and the value for each pixel is normalized by the total power. Since the scattering in the forested area at the L-band is mostly contributed by the volume component, the inferred horizontal orientation in the L-band image in Fig. 3-26 should be indicative of scattering by branches. However, the horizontal orientation in the P-band image is not related to the physical orientation of scatterers in the volume layer. It is well-known that the double-bounce scattering raises the HH contribution due to the Fresnel reflections at

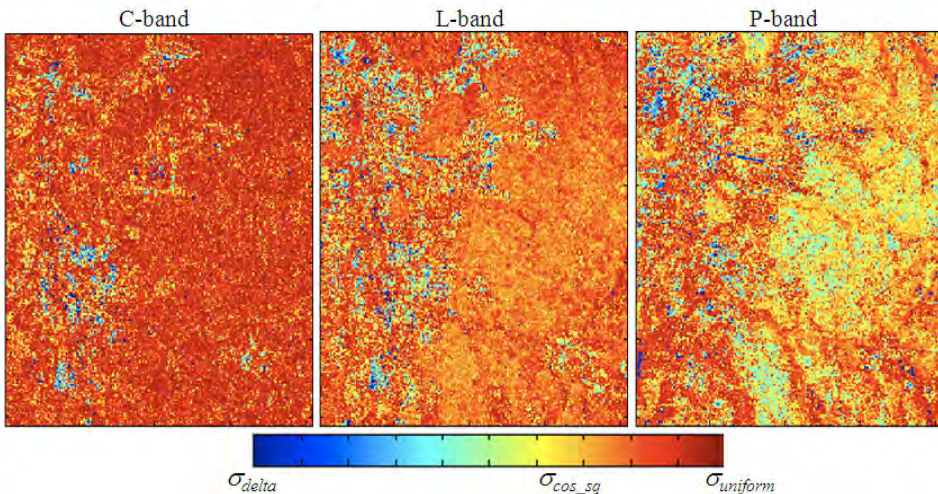


Fig. 3-25. Randomness maps derived from the C-band (left), L-band (center), and P-band (right) AIRSAR images in the Black Forest. As in the numerical example, the randomness decreases for the longer wavelengths (Arii et al., 2009 [16]).

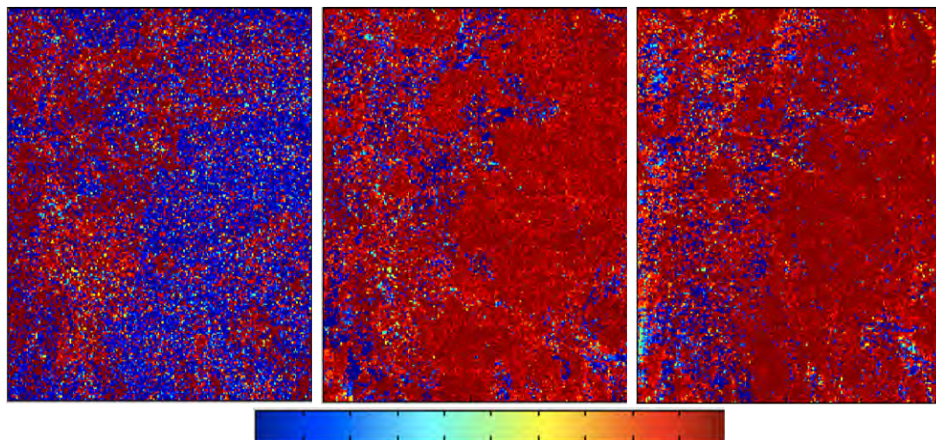


Fig. 3-26. Mean orientation angle maps derived from the C-band (left), L-band (center), and P-band (right) AIRSAR images in the Black Forest (Arii et al., 2009 [16]).

the trunk and ground surface. Since the algorithm subtracts the volume component first and then infers the other scattering mechanisms, strong double-bounce contribution misleads us to interpret a horizontally oriented volume component. One must pay particular attention to interpret the mean orientation angle map when double-bounce scattering contribution is dominant. The C-band mean orientation angle map indicates scattering from more vertically oriented scatterers. Given that the shorter C-band wavelength mostly interacts with the needles and mostly with those needles near the top of the canopy (scattering lower down in the canopy is expected to be attenuated), this result is reasonable.

A clear contrast exists along the river and road in the P-band in Fig. 3-27. The scattering from the forested area is basically contributed by both volume and double-bounce terms. However, the volume component is significant along the river and road, whereas the double-bounce is considerably smaller. This result is due to the local topography, as pointed out by van Zyl [5], where the double-bounce contribution is drastically reduced because the Fresnel reflections no longer dominate when the forest floor is tilted.

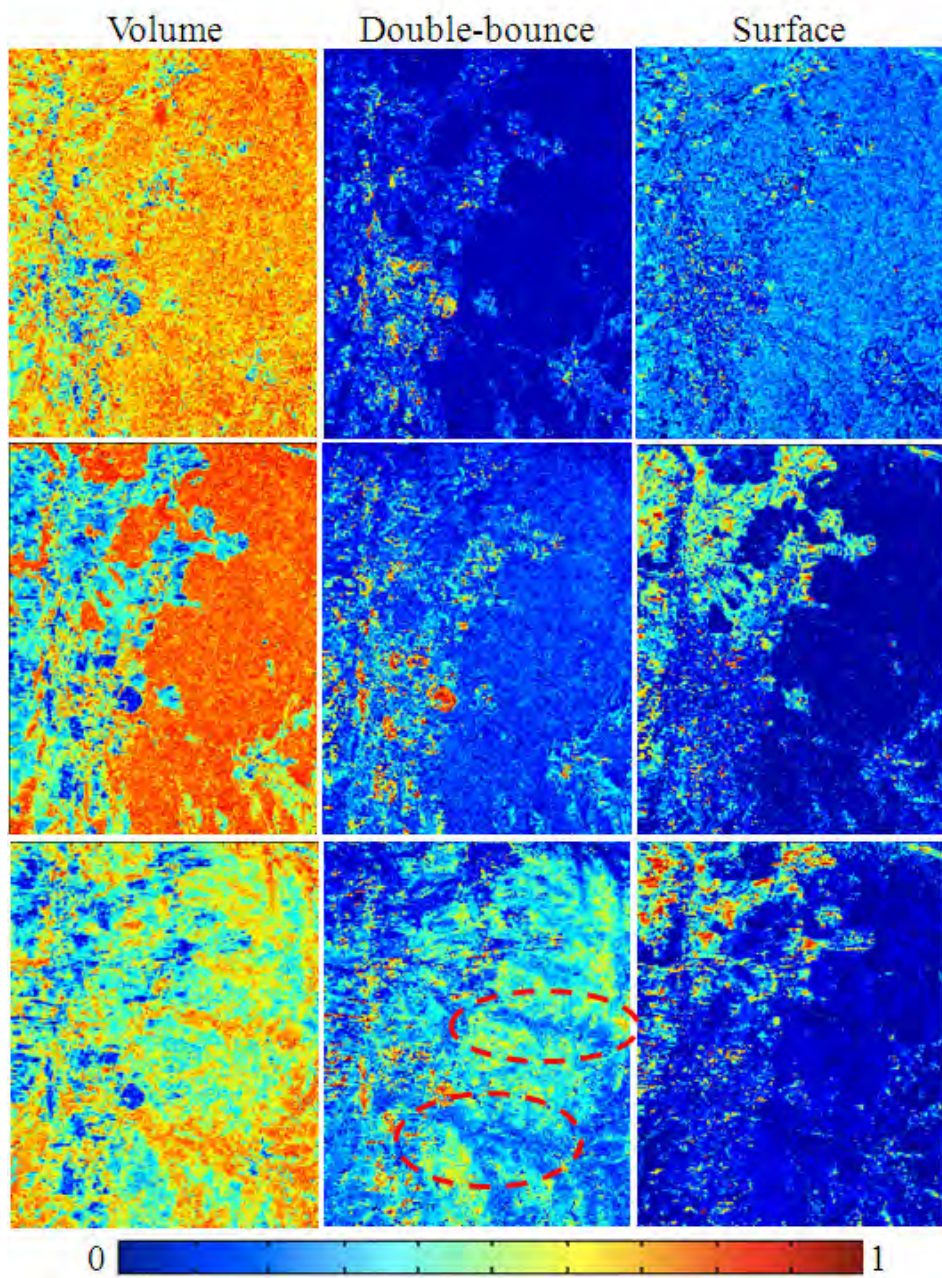


Fig. 3-27. Volume (left), double-bounce (center), and surface (right) components of the adaptive algorithm for the C-band (top), L-band (middle), and P-band (bottom) Black Forest images. Each pixel is normalized by total power. Dotted lines in red indicate river (upper) and road (lower), respectively (Arii et al., 2009 [16]).

3.4 Image Classification

Classification of images involves using a set of rules to decide whether different pixels in an image have similar characteristics. These rules in effect divide the total data space into subsets separated by so-called decision boundaries. All pixels that fall within a volume surrounded by such decision boundaries are then labeled as belonging to a single class.

Two major approaches are used in classifying images; supervised and unsupervised classifications. In the case of supervised classification, a user will specify so-called feature vectors to be used in the comparison process. These vectors can be thought of as defining the centroids of the decision volumes that are separated by the decision boundaries. These feature vectors can be extracted from the image to be classified, or could come from a library of radar signatures either measured in the laboratory or in the field. In the case of unsupervised classification, the computer is allowed to find the feature vectors without help from an image analyst. In the simplest form, known as the *K-means algorithm*, K feature vectors are typically selected at random from the data space.

A different way to look at classification approaches is whether they are based purely on the data available in the image, or whether the analyst is adding information based on physics. The former is often referred to as a statistical approach, or more correctly, a data driven approach. The analyst relies purely on the data and the statistics associated with the data to segment the image into classes. In the physics-based approach, the analyst compares the data in the image to known characteristics based on physics. For example, one might be interested in knowing which parts of a scene are covered with vegetation. Based on the physics of vegetation scattering models, one might conclude that such areas would exhibit relatively large entropy or RVI values, and use those parameter with some threshold value to decide whether a pixel should be labeled as vegetated or not.

3.4.1 Supervised Classification

The most popular supervised classification technique is the Bayes classifier. The basic principle of the Bayes classifier can be described using Eqs. (3.4-1) and (3.4-2). If a land class is denoted by ϖ_i where $i = 1, 2, \dots, N$ classes, a pixel A can be classified as

$$A \in \varpi_i \text{ if } P(\varpi_i | A) > P(\varpi_j | A). \quad (3.4-1)$$

However, it is much easier to evaluate $P(A | \varpi_i)$ than $P(\varpi_i | A)$ using ground-truth data. Therefore, we transform Eq. (3.4-1) using the Bayes theorem as

$$A \in \varpi_i \text{ if } P(A|\varpi_i)P(\varpi_i) > P(A|\varpi_j)P(\varpi_j). \quad (3.4-2)$$

It is convenient to transform Eq. (3.4-2) using a distance measure $d_i(A)$ as

$$A \in \varpi_i \text{ if } d_i(A) < d_j(A). \quad (3.4-3)$$

where, typically

$$d_i(A) = -\ln P(A|\varpi_i)P(\varpi_i). \quad (3.4-4)$$

Using Eqs. (3.4-3) and (3.4-4), pixel A is classified to be ϖ_i if the distance measure of ϖ_i ($= -\ln P(A|\varpi_i)P(\varpi_i)$) is the shortest among all possible classes. As the simplest example, if the conditional probability density function (PDF) derived from the ground truth data is given by the normal distribution as

$$P(A|\varpi_i) = \frac{1}{\sqrt{2\pi}s_i} \exp\left[-(A - \mu_i)^2 / 2s_i^2\right]. \quad (3.4-5)$$

where μ_i and s_i are the mean value and the standard deviation of the conditional PDF of the class ϖ_i . The distance measure can be calculated as

$$d_i(A) = \left[(A - \mu_i) / \sqrt{2}s_i \right]^2 + \ln(s_i) - \ln P(\varpi_i). \quad (3.4-6)$$

The most challenging step of evaluating Eq. (3.4-6) is to estimate $P(\varpi_i)$ for all classes before we apply a classification method to polarimetric SAR data. One commonly used assumption is that an equal probability is assigned to all classes. Then, Eq. (3.4-6) can be simplified as

$$d_i(A) = \left[(A - \mu_i) / \sqrt{2}s_i \right]^2 + \ln(s_i). \quad (3.4-7)$$

From Eq. (3.4-7), the distance measure becomes smaller if the distance (normalized by the standard deviation of PDF) between the measured pixel value and the PDF mean value is smaller.

For the fully polarimetric SAR case, Lim et al. (1989) [19] calculated the distance measure as

$$d_i(\mathbf{X}) = \mathbf{X}^+ [\mathbf{C}]_i^{-1} \mathbf{X} + \ln |[\mathbf{C}]_i| - \ln P(\varpi_i). \quad (3.4-8)$$

where the complex vector \mathbf{X} is given by

$$\mathbf{X} = \begin{bmatrix} S_{hh} \\ S_{hv} \\ S_{vv} \end{bmatrix}; [\mathbf{C}]_i = \langle \mathbf{X}_i \mathbf{X}_i^+ \rangle. \quad (3.4-9)$$

Here $[\mathbf{C}]_i$ is the covariance matrix of the assumed class feature for the i th class. The conditional PDF is given by

$$P(\mathbf{X} | \varpi_i) = \frac{1}{\pi^3 |[\mathbf{C}]_i|} \exp\left(-\mathbf{X}^+ \cdot [\mathbf{C}]_i^{-1} \cdot \mathbf{X}\right). \quad (3.4-10)$$

The complex Gaussian distribution given in Eq. (3.4-10) is a good approximation for single-look polarimetric data. Lee et al. [20] showed that for multi-look polarimetric SAR data, the complex Wishart distribution is a better approximation. Using this distribution, Lee *et al.* derived the following distance measure

$$d_i(\mathbf{Z}) = n \left[\ln |[\mathbf{C}]_i| + \text{Tr}(\mathbf{C}_i^{-1} \mathbf{Z}) - \ln P(\varpi_i) \right]. \quad (3.4-11)$$

Here \mathbf{Z} represents the covariance matrix of the pixel being classified, and n is the number of looks in the image.

To implement Eq. (3.4-8) or (3.4-11), one must evaluate all $P(\varpi_i)$ or assume equal *a priori* probabilities for all the classes. In the absence of any additional information equal *a priori* probabilities are often assumed. Figure 3-28 shows an example of a supervised Bayesian classification of the Black Forest image we analyzed earlier in the chapter. Here we selected three training sets, one in the agricultural area (displayed in blue), one in the urban area (displayed in red), and one in the forested area (displayed in green). The image on the left in Fig. 3-28 shows the result using the full covariance matrix, including the absolute radar cross-section assuming equal *a-priori* probabilities. The results show that most of the agricultural area is in fact identified as similar to that training area, and similarly for the other two classes. A closer look at the top right-hand corner of the image on the left shows a diagonal line of red pixels, meaning these pixels were classified as being similar to the urban training area. The scattering in this area is not similar to double reflects, however. These pixels were placed in this class mainly because of their large absolute cross-sections.

The image on the right in Fig. 3-28 repeats the calculation, but this time using the normalized covariance matrices. In other words, all brightness information was discarded, and the classification is done purely on the relative strength of

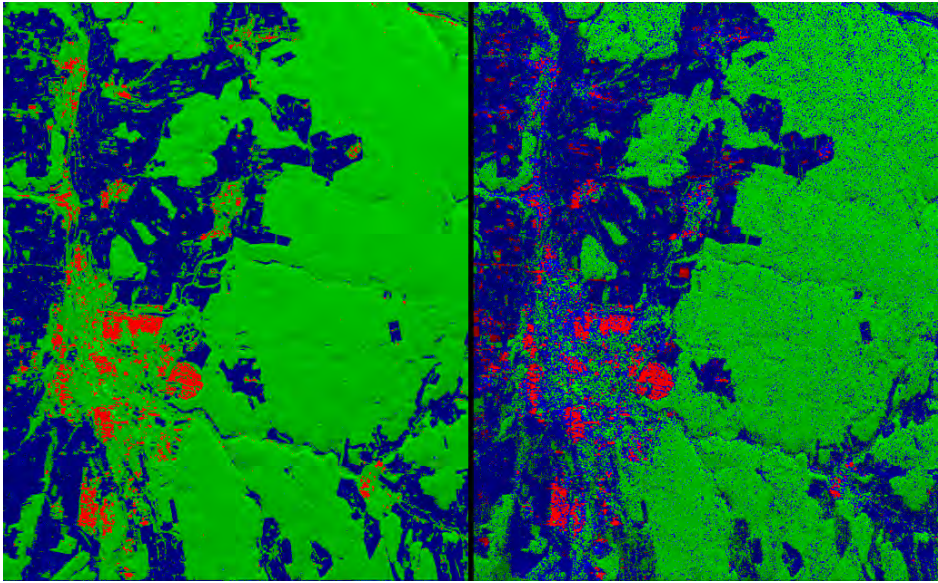


Fig. 3-28. Bayesian classifications of the L-band Black Forest image using training areas in the agricultural area (blue), urban area (red) and the forest (green). The image on the left uses the absolute brightness, while the one on the right uses normalized covariance matrices. See the text for a discussion.

the polarimetric information. Overall, the general results between the two images are similar. However, closer examination of the image on the right shows that several areas, particularly in the agricultural areas, are classified differently. Since the polarimetric information is more directly related to the scattering mechanisms, we expect the image on the right to show more details about the scattering mechanisms. For example, the diagonal line of red pixels in the upper right is now correctly identified as similar to the forest training area. Note, however, that the classification on the right appears noisier than the left.

In calculating the result shown in Fig. 3-28, we assumed equal *a-priori* probabilities for each of the classes. In the absence of additional information, this is a reasonable assumption. Van Zyl and Burnette (1992) [21] proposed an iterative method to evaluate $P(\varpi_i)$. First, they assume equal probabilities for all $P(\varpi_i)$. Then, the results from the first classification (equal probability assumption) are used to estimate all $P(\varpi_i)$. This is done by calculating the number of pixels in a pre-determined box that was placed in each class, divided by the total number of pixels in the box. The successive iteration improves the accuracy of the classification. Rignot and Chellappa (1992) [22] proposed a maximum *a posteriori* (MAP) estimate to segment polarimetric SAR data. The segmentation results using MAP showed a 10–20 percent improvement when

they are compared with the results using the maximum likelihood (ML) method under the equal probability assumption.

Figure 3-29 shows the result of applying the iterative scheme proposed by van Zyl and Burnette to estimate the probabilities for each class. On the left is the original Bayes classification with equal *a-priori* probabilities. On the right is the result after a single iteration using a 5×5 box to calculate the probability of finding a specific class in a given pixel. The result is a dramatic decrease in the apparent noise in the classification. Van Zyl and Burnette found that in general very few iterations are needed for the classification to converge [21].

In order to improve the classification accuracy, SAR images are often filtered to suppress speckle noise. Lee et al. (1999) [23] proposed a technique to preserve polarimetric properties without degrading the image quality. To avoid the crosstalk between polarimetric channels, each element of the covariance matrix was filtered independently. The filtering was performed by averaging the covariance matrix of neighboring pixels without deficiency of smearing the edges. To preserve the edge sharpness, the filtering was adaptively applied to a homogeneous area from selected neighboring pixels using edge-aligned windows [23]. Using this filtering, Lee et al. (1999) [23] reported that the classification accuracy was approximately doubled for five classes out of the

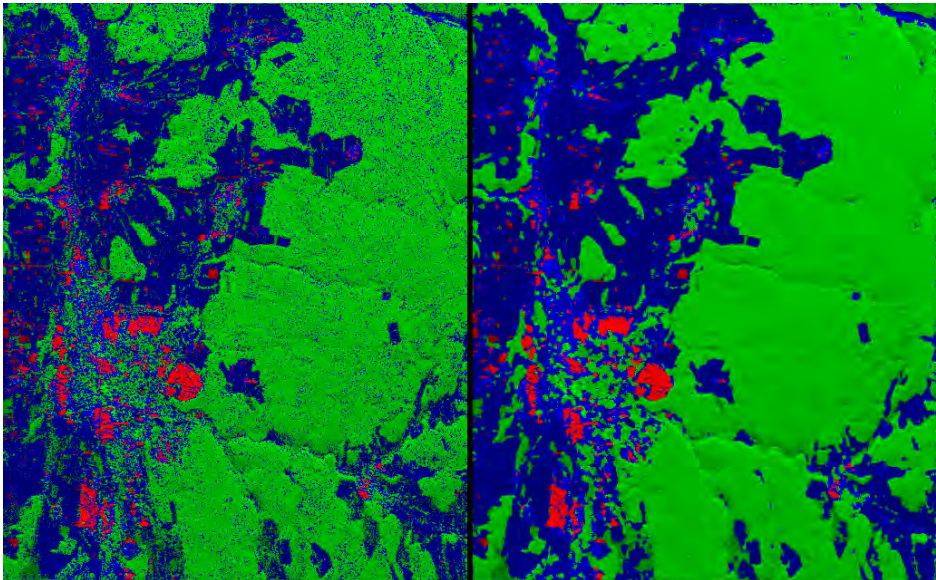


Fig. 3-29. The image on the left was classified using equal *a-priori* probabilities for all classes, and normalized covariance matrices. The image on the right illustrates the result of using adaptive *a-priori* probabilities as proposed by van Zyl and Burnette to perform the classification. The image on the left is used with a 5×5 box centered on each pixel to calculate the probability of finding a specific class in that pixel. The image on the right is the result of a single iteration.

total of seven classes when the results were compared with the ones using the data without any filtering.

3.4.2 Physics-Based Unsupervised Classification

Supervised classifications allow the analyst to select feature vectors from the image itself and then use them on the Bayesian algorithm to identify which pixels in the image are the closest to the selected features. One difficulty with this approach is that the results are dependent on how well the person picks the class training areas. If the selected areas are not very homogeneous, the results may not be very satisfying. A different type of approach relies on physics to segment a polarimetric image into different classes of scattering. This approach is completely unsupervised, and does not rely on a human to pick areas to use as the class centroids.

One of the earliest polarimetric unsupervised classification schemes was suggested by van Zyl [24]. Pixels in an image are compared to three scattering mechanisms, odd numbers of reflections, even numbers of reflections, and diffuse scattering based on the expected scattering parameters predicted by simple models. The results showed that bare surfaces are usually similar to the odd number of reflections model, while urban areas typically scatter consistent with an even-number-of-reflections model. Vegetated areas mostly exhibit diffuse scattering, particularly at longer wavelengths. This interpretation is confirmed by the results shown in Fig. 3-30.

This idea was taken further by Cloude and Pottier [25] using the entropy and average alpha angle discussed earlier to divide the data space into nine different regions. They showed that of these nine regions, eight are commonly found in polarimetric radar data. Based on this division of the data space, one can then segment the image based on which region in the data space each pixel falls into. As in the case of van Zyl, this algorithm requires no user input, and the segmentation is done automatically. Results show that the two classes with the largest entropy are similar to the diffuse scattering class defined by van Zyl [24]. The alpha-entropy classification further segments van Zyl's odd numbers of reflections and even number of reflections classes into several classes based on the amount of randomness in the scattering as measured by the entropy. See Fig. 3-30 for the results of this algorithm when applied to the L-band Black Forest image.

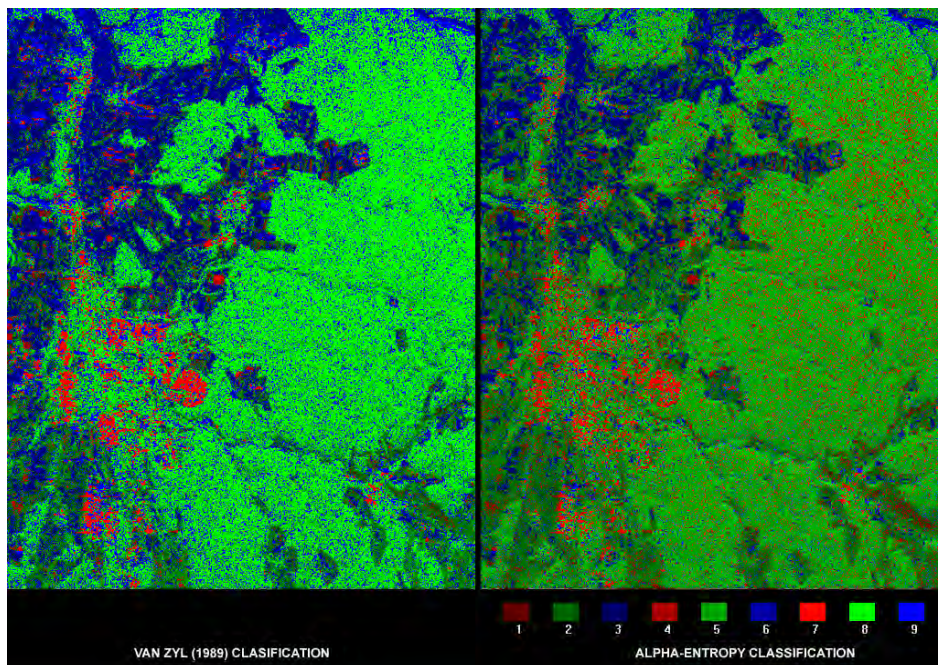


Fig. 3-30. Unsupervised classifications of the L-band image of the Black Forest using the algorithm by van Zyl [24] (left) and the alpha-entropy algorithm (right). The alpha-entropy image further divides the original three classes using the entropy information.

3.4.3 Combined Unsupervised and Bayes Classification Algorithms

As mentioned above, it is difficult to find reliable training data sets to estimate the statistical parameters required for the maximum likelihood classification. To overcome this difficulty, some authors have proposed using an unsupervised classification technique to produce initial training data sets. Lee et al. (1999) [26] proposed an unsupervised classification technique that combines a polarimetric decomposition method (unsupervised) and the complex Wishart classifier [20] (supervised). The “alpha-entropy” algorithm [25, 27] based on the polarimetric decomposition technique was used to provide the initial training data set for the eight zones defined by the alpha angle and the entropy. This training data set was used as an input for the Wishart classifier. The classification result was improved by iteration of this process. When the iteration process satisfies some pre-determined termination criteria, the classification result is finalized.

More recently, Lee et al. (2004) [27] proposed a different approach to combine both unsupervised and supervised classification techniques. In this approach, they applied the model-based decomposition algorithm by Freeman and Durden [9] to the polarimetric SAR data to provide the classification result for three

categories: surface, double bounce, and volume scattering mechanisms. This division was accomplished based on the dominant power associate with each scattering mechanism. Lee et al. (2004) [27] divided each category into 30 clusters based on the backscattering power of their dominant scattering mechanism. The initial clusters were merged based on the between-cluster Wishart distance [27] to form the classes. The Wishart classification method was applied to the polarimetric data iteratively until this process converged. These combined classification approaches usually provide more accurate classification results than unsupervised approach can without requiring the ground truth data.

Figure 3-31 illustrates the idea behind a combined unsupervised and Bayesian classification algorithm. In this example, we used three model-derived covariance matrices to perform the initial unsupervised classification. The three

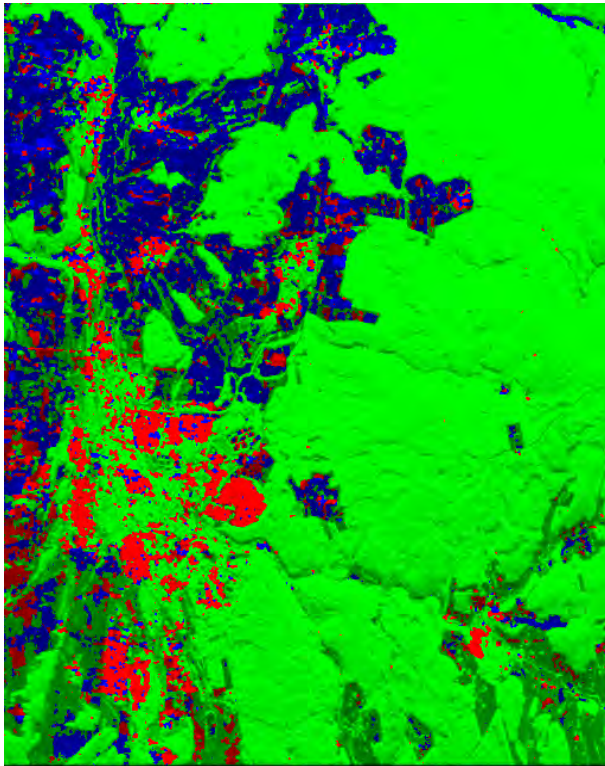


Fig. 3-31. Results using three model-derived covariance matrices to perform an unsupervised classification of the L-band Black Forest data. Pixels displayed in red are similar to a double reflection expected from two dielectric surfaces, those in blue are similar to a bare rough surface, and those in green are similar to a cloud of uniformly oriented thin dielectric cylinders.

models are that of a rough bare surface, a dihedral corner reflector with dielectric surfaces, and a uniformly randomly oriented cloud of thin cylinders. These three model covariance matrices are used in an unsupervised classification using normalized covariance matrices. Once the initial classification is performed, the average covariance matrix for each class is calculated and used in the next step. This process is iterated until the classification converges in the sense that less than .001 percent of the pixels still change class.

We note that there is great similarity between this unsupervised classification and the supervised classification using normalized covariance matrices shown on the right in Fig. 3-28. The main difference is that more areas in the agricultural areas are classified as being more similar to the dielectric dihedral reflection.

One drawback of all classification algorithms is that they force a pixel to belong to one class only. The decision is based on which class most closely resembles the observed scatter. Unfortunately, scattering is seldom purely one mechanism. As we shall see in Chapter 5, scattering from vegetated areas often is a mixture of many different scattering mechanisms. Forcing a pixel to belong to one class ignores this reality. We therefore believe that classification results should be interpreted with care. Our personal preference is to use techniques that preserve the relative fractions of different scattering mechanisms, such as the Pauli matrix decomposition or one of the model-based decompositions.

3.5 Polarimetric SAR Interferometry

SAR interferometry refers to a class of techniques where additional information is extracted from SAR images that are acquired from different vantage points, or at different times. Various implementations allow three types of information to be extracted: 1) topography, 2) surface velocity, and 3) surface deformation. If two SAR images are acquired from slightly different viewing geometries, information about the topography of the surface can be inferred. Conversely, if images are taken at slightly different times, a map of surface velocities can be produced. Finally, if sets of interferometric images are combined, subtle changes in the scene can be measured with extremely high accuracy. These techniques are summarized in more detail in several references [28, 29, 30].

SAR interferometry was first demonstrated by Graham (1974) [31], who demonstrated a pattern of nulls or interference fringes by vectorially adding the signals received from two SAR antennas; one physically situated above the other. Later, Zebker and Goldstein (1986) [32] demonstrated that these interference fringes can be formed after SAR processing of the individual

images if both the amplitude and the phase of the radar images are preserved during the processing.

The basic principles of interferometry can be explained using the geometry shown in Fig. 3-32. Two radar return signals ($E(A_1)$ and $E(A_2)$) are recorded by the two interferometric antennas (A_1 and A_2 shown in Fig. 3-32) separated by the baseline B . A 2x2 Hermitian matrix can be formed using $E(A_1)$ and $E(A_2)$ as

$$[I_n] = \begin{pmatrix} E(A_1) \\ E(A_2) \end{pmatrix} \begin{bmatrix} E(A_1)^* & E(A_2)^* \end{bmatrix} = \begin{pmatrix} \langle E(A_1)E(A_1)^* \rangle & \langle E(A_1)E(A_2)^* \rangle \\ \langle E(A_2)E(A_1)^* \rangle & \langle E(A_2)E(A_2)^* \rangle \end{pmatrix} \tag{3.5-1}$$

The diagonal components represent two conventional SAR images collected by the interferometric SAR system. The interferometric SAR information can be extracted from the off diagonal component $\langle E(A_1)E(A_2)^* \rangle$. The phase of this term (known as interferogram) is defined as

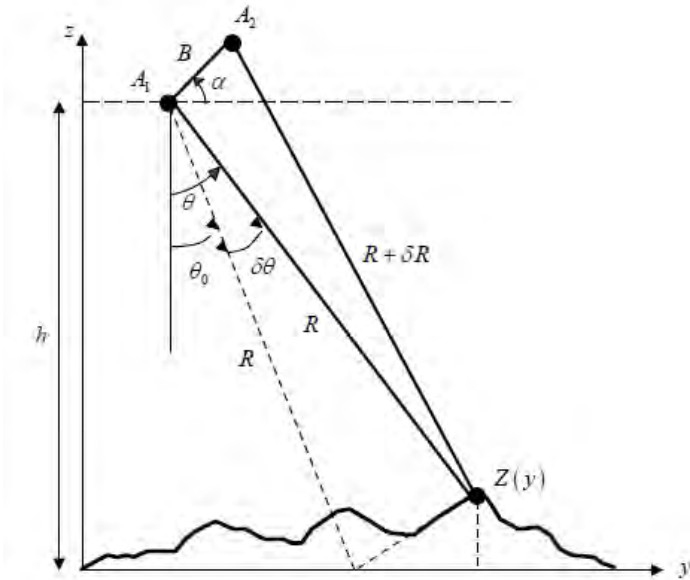


Fig. 3-32. Basic interferometric radar geometry. The path length difference between the signals measured at each of the two antennas is a function of the elevation of the scatterer. (From Elachi and van Zyl (2006) [28])

$$\phi_I = \arg \left\{ \left\langle E(A_1) E(A_2)^* \right\rangle \right\}. \quad (3.5-2)$$

Radar interferometry can be implemented in two different ways. In so-called single-pass interferometers, the two antennas are physically separated, but on the same platform. In the case of airborne SAR systems, the two interferometric antennas might be mounted in different places on the fuselage, or under the wings of the aircraft. In the case of the Shuttle Radar Topography Mission (SRTM) that was flown on the Space Shuttle Endeavour in 2000, a 60 meter (m) long boom was used to separate the two antennas. Single-pass interferometers acquire the images from both ends of the baseline at the same time.

An alternative way to implement radar interferometry is to use images from different orbits in the case of spaceborne systems, or in the case of airborne systems, from different flight lines. This implementation is known as repeat-track interferometry. In this case, images at each end of the baseline are acquired at different times, with time separations varying from minutes in the case of airborne systems to days to even years in the case of spaceborne systems. A slight variation of the repeat-track implementation is to use two satellites that follow each other in slightly different orbits. This is known as tandem interferometry. The time difference for acquiring images is typically seconds to minutes, depending on how far apart the two satellites are positioned.

The scattering center of a pixel can be located using the law of cosines on the triangle formed by the two antennas and the scattering center of a pixel as

$$(R + \delta R)^2 = R^2 + B^2 - 2BR \cos\left(\frac{\pi}{2} - \theta + \alpha\right). \quad (3.5-3)$$

The variables in Eq. (3.5-3) are shown in Fig. 3-32. If we assume that $R \gg B$, (a very good assumption for most interferometers) one finds that

$$\delta R \approx -B \sin(\theta - \alpha). \quad (3.5-4)$$

The radar system does not measure the path length difference explicitly, however. Instead, what is measured, is an interferometric phase difference that is related to the path length difference through

$$\phi_I = \phi_I + 2\pi N = \frac{a2\pi}{\lambda} \delta R = -\frac{a2\pi}{\lambda} B \sin(\theta - \alpha). \quad (3.5-5)$$

where $a=1$ for the case where signals are transmitted out of one antenna and received through both at the same time, and $a=2$ for the case where the signal

is alternately transmitted and received through one of the two antennas only. In order to reconstruct the topography, the integer N must be determined using a phase unwrapping technique [33, 34].

From Fig. 3-32, it also follows that the elevation of the point being imaged is given by

$$z(y) = h - R \cos \theta = h - R \cos \left[\alpha - \sin^{-1} \left(\frac{\lambda \phi_T}{a2\pi B} \right) \right]. \quad (3.5-6)$$

with h denoting the height of the reference antenna above the reference plane with respect to which elevations are quoted. As shown in Eq. (3.5-6), the interferometric phase (ϕ_T) provides the information on the location of the scattering center. Since the return signals from two interferometric antennas are collected in a different geometry, there is decorrelation between two signals. This decorrelation can provide the additional information on scattering objects to be imaged.

The interferometric coherence is defined as

$$\gamma_{INT} = \frac{\left| \left\langle E(A_1) E(A_2)^* \right\rangle \right|}{\sqrt{\left\langle E(A_1) E(A_1)^* \right\rangle \left\langle E(A_2) E(A_2)^* \right\rangle}} = \gamma_{SNR} \gamma_T \gamma_B. \quad (3.5-7)$$

The interferometric decorrelation is composed of three contributions: 1) additive noise, 2) slightly different imaging geometry of two antennas, and 3) temporal changes of scattering objects. As shown in Eq. (3.5-7), γ_{SNR} includes decorrelation due to additive noise. If both interferometric channels have the same SNR, γ_{SNR} can be written as

$$\gamma_{SNR} = \frac{1}{1 + \frac{1}{SNR}}. \quad (3.5-8)$$

The temporal correlation (γ_T) represents the scattering geometry change in time [35]. If the interferometric signals are collected at the same time, $\gamma_T=1$. The baseline decorrelation ($1-\gamma_B$) is due to the speckle difference due to the fact that two interferometric signals are collected in a slight different imaging geometry. This term (γ_B) includes the information on scattering objects. If the scattering object is a point target, there is no baseline decorrelation. The baseline decorrelation is a key parameter to understand the scattering

characteristic of each pixel. The baseline correlation (γ_B) can be estimated from the measured correlation coefficient (γ) after removing the effect of γ_{SNR} and γ_T as shown in (3.5-7). The expression for the baseline correlation to estimate the scattering characteristic of each pixel can be found in [29].

Electromagnetic wave propagation is by nature a vector phenomenon. Therefore, in order to capture the complete information about the scattering process, interferometric measurements should really be made in the full polarimetric implementation of a radar system. In this case, there are really three different measurements being made at the same time. First, there are the two polarimetric radar measurements at each end of the baseline, represented below by the two covariance matrices $[\mathbf{C}_{11}]$ and $[\mathbf{C}_{22}]$. Since the baseline is generally short compared to the distance to the scene, these two measurements can be expected to be nearly identical, except for the very small change in the angle of incidence from one end of the baseline to the other. The third measurement, of course, is the full vector interferogram as opposed to the scalar implementation described earlier.

The vector interferogram, which is the complex cross-correlation of the signal from one end of the baseline with that from the other end of the baseline, can be described as

$$V_1 V_2^* = \tilde{\mathbf{A}}_1 \mathbf{T}_1 \tilde{\mathbf{T}}_2^* \mathbf{A}_2^* = \mathbf{A}_1 \cdot [\mathbf{C}_{12}] \mathbf{A}_2^*. \quad (3.5-9)$$

The antenna (\mathbf{A}) and scatterer (\mathbf{T}) vectors are given in Eq. (3.1-1). The complex correlation of the two signals after averaging is

$$\mu = \frac{\langle V_1 V_2^* \rangle}{\sqrt{\langle V_1 V_1^* \rangle \langle V_2 V_2^* \rangle}} = \frac{\mathbf{A}_1 \cdot \langle [\mathbf{C}_{12}] \rangle \mathbf{A}_2^*}{\sqrt{(\mathbf{A}_1 \cdot \langle [\mathbf{C}_{11}] \rangle \mathbf{A}_1^*) (\mathbf{A}_2 \cdot \langle [\mathbf{C}_{22}] \rangle \mathbf{A}_2^*)}}. \quad (3.5-10)$$

Notice that the interferometric phase is a function of the antenna polarization vectors as shown in Eq. (3.5-9).

$$\phi_{\text{int}} = \arg(\mathbf{A}_1 \cdot \langle [\mathbf{C}_{12}] \rangle \mathbf{A}_2^*). \quad (3.5-11)$$

Notice that the interferometric phase will be used to locate the scattering center of different antenna polarization combinations. In addition, the polarimetric correlation coefficient can be used to estimate the scattering characteristics of each pixel. Using this formulation, Cloude and Papathanassiou (1998) [36] showed, using repeat-track SIR-C interferometric data, that polarization diversity can be used successfully to optimize the correlation between images.

They also showed significant differences in the measured elevation in forested areas when using polarization optimization. At present, polarimetric interferometry is a very active research area [37, 38, 39, 40, 41, 42]. Unfortunately, progress is hampered severely by lack of availability of well-calibrated data, as only a hand-full of radar systems have been upgraded to full polarimetric interferometry capability.

To illustrate the information content of polarimetric interferometry, we used data acquired in the repeat-track interferometry mode using the SIR-C system when it flew on the Space Shuttle in October 1994. The data we use were acquired over the Mahantango Watershed near Harrisburg, Pennsylvania. An L-band total power image of part of the area is shown in Fig. 3-33. The Mahantango watershed is part of the Valley and Ridge Physiographic Province of eastern Pennsylvania. The area is characterized by forested ridge tops, while



Fig. 3-33. L-band total power image of a portion of the Mahantango watershed in Pennsylvania. The darker areas are agricultural fields, and the brighter grey tones are forested ridge tops.

the valley areas are typically used for agriculture. Approximately 55 percent of the area is forested, and about 45 percent of the area is used for cropland.

To illustrate the additional information contained in the polarimetric data, we choose to display differential interferograms using the image on the left in Fig. 3-34. The differential interferograms are constructed as follows. First we construct the HH interferogram as the reference. We then construct interferograms that are effectively the phase of each of the covariance matrix elements in Eq. (3.5-9). We then subtract the HH interferogram phase from each of these to form nine differential interferograms. These are shown in Fig. 3-34.

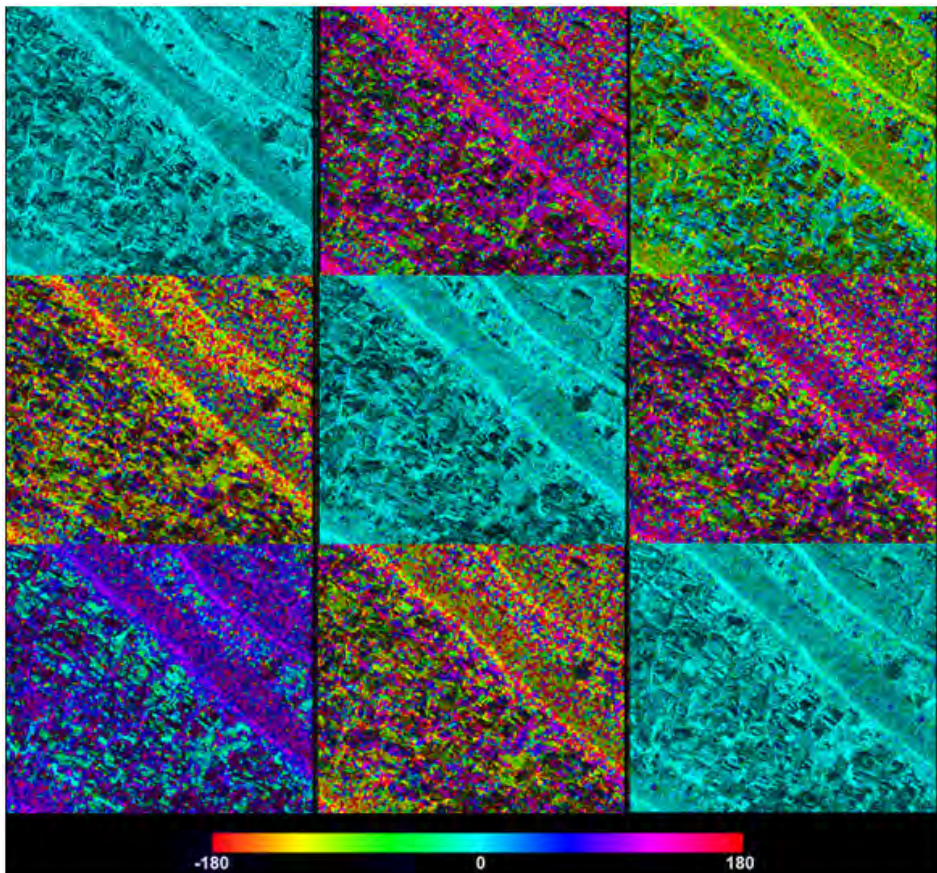


Fig. 3-34. Differential interferograms constructed using the polarimetric information acquired over the Mahantango watershed. The top row represent HH polarization on pass one, and HH on pass two (left), HV on pass two (middle) and VV on pass two (right). The second row is the same, except for HV on pass one, and the third row represents VV on pass one. See the text for how these were generated. Images across the upper left lower right diagonal are the complex conjugates of each other, hence the different colors.

The most striking is the image in the upper right in Fig. 3-34, which displays the differential phase of using HH polarization at one antenna and VV polarization at the other. The image shows that the agricultural areas in general have almost zero phase (which means they have the same phase in the VV and the HH interferogram). The forested areas, however, shows a significant phase angle, in this case near 90 deg.

3.6 Summary

In this chapter we introduced several more advanced polarimetric concepts. The vector-matrix duality allows us to understand decomposition algorithms in more detail. We also discussed several parameters based on the eigenvalues of the covariance matrix. These parameters provide useful information concerning the amount of randomness in the observed scatter, as well as potentially what the actual scattering mechanisms might be.

Finally, we examined different approaches for interpreting the scattering mechanisms in an image. Using orthogonal bases, we can derive unique decompositions. These decompositions, while unique, are not straightforward to interpret. In particular, the decomposition based on the eigenvectors of the covariance matrix suffers from the fact that the basis in which the decomposition is done varies from pixel to pixel in the image. This further complicates the interpretation. At the other end of the spectrum are model-based decompositions. These are not unique, and picking the appropriate solution is not obvious, but their interpretation is more straightforward. We showed that some of the popular model-based decompositions suffer from serious limitations imposed by the assumptions of how the observations are to be decomposed; these assumptions lead to results that are non-physical in the sense that negative powers could be generated. We showed that this limitation can easily be removed using a simple check based on the eigenvalues of the covariance matrix. A simple hybrid approach can be implemented that corrects these limitations. This approach is then easily extended to show a simple way to find the best model to fit the observed canopy scattering.

It is important to remember that all these decomposition techniques are simply tools to make interpretation of the observed scattering easier. The strength of the pure eigenvalue and eigenvector approaches is that the answers are unique, and no assumptions are required to perform the decomposition. The interpretation of the results, however, requires an interpretation of the basis vectors in terms of scattering mechanisms, which might not be unique. The model-based decompositions provide an easy interpretation. But this easy interpretation assumes that the models are indeed applicable to the observations, which might not be the case. Furthermore, the results are not

unique in the sense that many different model combinations could be used. In the final analysis, which tool is used depends on personal preference.

References and Further Reading

- [1] S. R. Cloude, "Uniqueness of target decomposition theorems in radar polarimetry," *Direct and Inverse Methods in Radar Polarimetry*, Part 1, NATO-ARW, W.M. Boerner, L. A. Cram, W. A. Holm, D. E. Stein, W. Wiebeck, W. Keydel, D. Giuli, D. T. Gjessing, F. A. Molinet, and H. Brand, eds., Kluwer Academic Publishers, Norwell, Massachusetts, pp. 267–296, 1992.
- [2] S. R. Cloude and E. Pottier, "The Concept of Polarization Entropy in Optical Scattering," *Optical Engineering*, vol. 34, no. 6, ISSN 0091-3286, pp. 1599–1610, 1995.
- [3] S. L. Durden, J. J. van Zyl and H. A. Zebker, "The Unpolarized Component in Polarimetric Radar Observations of Forested Areas," *IEEE Transactions on Geoscience and Remote Sensing*, vol. GE-28, no. 2, pp. 268–271, 1990.
- [4] Y. Kim and J. van Zyl, "Comparison of Forest Estimation Techniques Using SAR Data," *Proceedings of IGARSS2001 Conference*, Sydney, Australia, IEEE (CDROM), 2001.
- [5] J. J. van Zyl, "The Effect of Topography on Radar Scattering from Vegetated Areas," *IEEE Transactions on Geoscience and Remote Sensing*, vol. GE-31, no. 1, pp. 153–160, 1993.
- [6] S. R. Cloude and E. Pottier, "A Review of Target Decomposition Theorems in Radar Polarimetry," *IEEE Transactions on Geoscience and Remote Sensing*, vol. GE-34, no. 2, pp. 498–518, 1996.
- [7] E. Krogager, *Aspects of Polarimetric Radar Imaging*, Ph.D. thesis, Technical University of Denmark, Copenhagen, 1993.
- [8] M. Borgeaud, R. T. Shin, and J. A. Kong, "Theoretical models for polarimetric radar clutter," *Journal of Electromagnetic Waves and Applications*, vol. 1, pp. 73–91, 1987.
- [9] A. Freeman and S. Durden, "A Three Component Scattering Model for Polarimetric SAR Data," *IEEE Transactions on Geoscience and Remote Sensing*, vol. GE-36, no. 3, pp. 963–973, 1998.
- [10] Y. Yamaguchi, T. Moriyama, M., Ishido, and H. Yamada, "Four-Component Scattering Model for Polarimetric SAR Image Decomposition," *IEEE Transactions on Geoscience and Remote Sensing*, vol. GE-43, no. 8, pp. 1699–1706, 2005.

- [11] D. L. Schuler, J-S. Lee, and G. De Grandi, "Measurement of Topography Using Polarimetric SAR Images," *IEEE Transactions on Geoscience and Remote Sensing*, vol. GE-34, no. 5, pp. 1266–1277, 1996.
- [12] J-S. Lee, D. L. Schuler, and T. L. Ainsworth, "Polarimetric SAR Data Compensation for Terrain Azimuth Slope Variation," *IEEE Transactions on Geoscience and Remote Sensing*, vol. GE-38, no. 5, pp. 2153–2163, 2000.
- [13] J. J. van Zyl, Y. Kim, and M. Arii, "Requirements for Model-Based Polarimetric Decompositions," *Proceedings of IGARSS2008 Conf.*, Vol. 5, IEEE International, Boston, Massachusetts, pp. 417–420, 2008.
- [14] J. J. van Zyl, M. Arii, and Y. Kim, "Model-Based Decomposition of Polarimetric SAR Covariance Matrices Constrained for Non-Negative Eigenvalues," *IEEE Transactions on Geoscience and Remote Sensing* (in press), 2010.
- [15] J. J. van Zyl, "Application of Cloude's Target Decomposition Theorem to Polarimetric Imaging Radar Data," *SPIE, Radar Polarimetry*, vol. 1748, pp. 184–212, 1992.
- [16] M. Arii, J. J. van Zyl, and Y. Kim, "Adaptive Model-Based Decomposition of Polarimetric SAR Covariance Matrices," *IEEE Transactions on Geoscience and Remote Sensing* (in press), 2010.
- [17] M. Arii, *Soil Moisture Retrieval under Vegetation Using Polarimetric Radar*, Ph.D. dissertation, California Institute of Technology, Pasadena, California, pp. 68–101, 2009.
- [18] M. Arii, J. J. van Zyl, and Y. Kim, "A General Characterization for Polarimetric Scattering from Vegetation Canopies," *IEEE Transactions on Geoscience and Remote Sensing* (in press), 2010.
- [19] H. H. Lim, A. A. Swartz, H. A. Yueh, J. A. Kong, and R. T. Shin, "Classification of Earth Terrain Using Polarimetric Synthetic Aperture Radar Images," *Journal of Geophysical Research*, vol. 94, no. B6, pp. 7049–7057, 1989.
- [20] J. S. Lee, M. R. Grunes, and R. Kwok, "Classification of Multi-Look Polarimetric SAR Imagery Based on Complex Wishart Distribution," *International Journal of Remote Sensing*, vol. 15, no. 11, pp. 2299–2311, 1994.
- [21] J. J. van Zyl and C. F. Burnette, "Bayesian Classification of Polarimetric SAR Images Using Adaptive *A Priori* Probabilities," *International Journal of Remote Sensing*, vol. 13, no. 5, pp. 835–840, 1992.
- [22] E. Rignot and R. Chellappa, "Segmentation of Polarimetric Synthetic Aperture Radar Data," *IEEE Transactions on Image Processing*, vol. 1, no. 3, pp. 281–300, 1992.

- [23] J. S. Lee, M. R. Grunes, and G. De Grandi, "Polarimetric SAR Speckle Filtering and Its Implication for Classification," *IEEE Transactions on Geoscience and Remote Sensing*, vol. 37, no. 5, pp. 2363–2373, 1999.
- [24] J. J. van Zyl, "Unsupervised Classification of Scattering Behavior Using Radar Polarimetry Data," *IEEE Transactions on Geoscience and Remote Sensing*, vol. 27, pp. 36–45, 1989.
- [25] S. Cloude and E. Pottier, "Entropy Based Classification Scheme for Land Applications," *IEEE Transactions on Geoscience and Remote Sensing*, vol. 35, pp. 68–78, 1997.
- [26] J. S. Lee, M. R. Grunes, T. L. Ainsworth, L. J. Du, D. L. Schuler, and S. R. Cloude, "Unsupervised Classification Using Polarimetric Decomposition and the Complex Wishart Classifier," *IEEE Transactions on Geoscience and Remote Sensing*, vol. 37, no. 5, pp. 2249–2258, 1999.
- [27] J. S. Lee, M. R. Grunes, E. Pottier, L. Ferro-Famil, "Unsupervised Terrain Classification Preserving Polarimetric Scattering Characteristics," *IEEE Transactions on Geoscience and Remote Sensing*, vol. 42, no. 4, pp. 722–731, 2004.
- [28] C. Elachi and J. van Zyl, *Introduction to the Physics and Techniques of Remote Sensing 2nd Edition*, Wiley-Interscience, Hoboken, New Jersey, pp. 268–283, 2006.
- [29] E. Rodriguez, J. M. Martin, "Theory and Design of Interferometric Synthetic Aperture Radars," *IEE Proceedings-F*, vol. 139, No.2, pp. 147–159, 1992.
- [30] P. A. Rosen, S. Hensley, I. R. Joughin, F. K. Li, S. N. Madsen, E. Rodríguez, and R. M. Goldstein, "Synthetic Aperture Radar Interferometry," *Proceedings of the IEEE*, vol. 88, pp. 333–382, 2000.
- [31] L. C. Graham, "Synthetic Interferometer Radar for Topographic Mapping," *Proceedings of the IEEE*, vol. 62, pp. 763–768, 1974.
- [32] H. Zebker and R. Goldstein, "Topographic Mapping from Interferometric SAR Observations," *Journal of Geophysical Research*, vol. 91, pp. 4993–4999, 1986.
- [33] R. M. Goldstein, H. A. Zebker, and C. Werner, "Satellite Radar Interferometry: Two-Dimensional Phase Unwrapping," *Radio Sci.*, vol. 23, pp. 713–720, 1988.
- [34] D. C. Ghiglia and L. A. Romero, "Direct Phase Estimation from Phase Differences Using Fast Elliptic Partial Differential Equation Solvers," *Optics Letters*, vol. 15, pp. 1107–1109, 1989.
- [35] H. A. Zebker and J. Villasenor, "Decorrelation in Interferometric Radar Echoes," *IEEE Transactions on Geoscience and Remote Sensing*, vol. 30, pp. 950–959, 1992.

- [36] S. R. Cloude and K. P. Papathanassiou, “Polarimetric SAR Interferometry,” *IEEE Transactions on Geoscience and Remote Sensing*, vol. 36, pp. 1551–1565, 1998.
- [37] R. N. Treuhaft and P. R. Siqueira, “Vertical Structure of Vegetated Land Surfaces from Interferometric and Polarimetric Radar,” *Radio Science*, vol. 35, pp. 141–177, 2000.
- [38] A. Reigber and A. Moreira, “First Demonstration of Airborne SAR Tomography Using Multibaseline L-band Data,” *IEEE Transactions on Geoscience and Remote Sensing*, vol. 38, pp. 2142–2152, 2000.
- [39] L. Sagues, J. M. Lopez-Sanchez, J. Fortuny, X. Fabregas, A. Broquetas, and A. Sieber, “Indoor Experiments on Polarimetric SAR Interferometry,” *IEEE Transactions on Geoscience and Remote Sensing*, vol. 38, pp. 671–684, 2000.
- [40] S. Sauer, L. Ferro-Famil, A. Reigber, and E. Pottier, “Polarimetric Dual-Baseline InSAR Building Height Estimation at L-band,” *IEEE Geoscience Remote Sensing Letters*, vol. 6, pp. 408–412, 2009.
- [41] I. Hajnsek, F. Kugler, S. Lee, and K. P. Papathanassiou, “Tropical-Forest-Parameter Estimation by Means of Pol-InSAR: The INDREX-II Campaign,” *IEEE Transactions on Geoscience and Remote Sensing*, vol. 47, pp. 481–493, 2009.
- [42] M. Neumann, L. Ferro-Famil, and A. Reigber, “Estimation of Forest Structure, Ground, and Canopy Layer Characteristics from Multibaseline Polarimetric Interferometric SAR Data,” *IEEE Transactions on Geoscience and Remote Sensing*, vol. 48, pp. 1086–1104, 2010.